Cell

Bispecific dendritic-T cell engager potentiates anti-tumor immunity

Graphical abstract

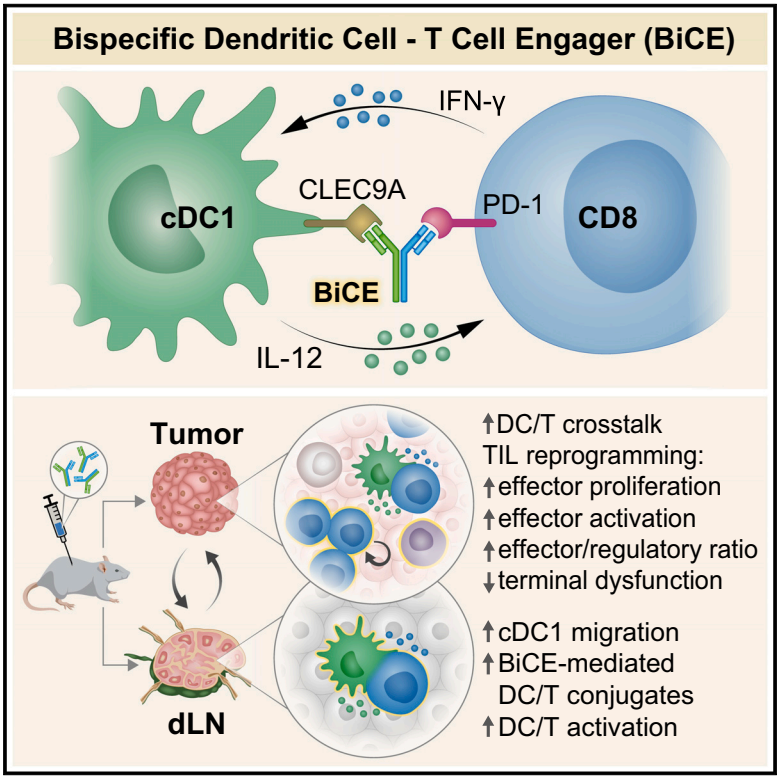

Highlights

- cDC1 are essential during the active phase of anti-PD1 treatment
- BiCE facilitates physical interactions of PD-1$^+$ T cells and XCR1$^+$ cDC1
- BiCE-mediated DC-T cell interactions exhibit a pro-inflammatory activation state
- BiCE treatment reprograms TILs and promotes potent anti-tumor immunity

Authors

Yuval Shapir Itai, Oren Barboy, Ran Salomon, ..., Amos Tanay, Ido Amit, Rony Dahan

Correspondence

ido.amit@weizmann.ac.il (I.A.), rony.dahan@weizmann.ac.il (R.D.)

In brief

A bispecific antibody that facilitates physical interactions between conventional type I dendritic cells and CD8$^+$ PD-1$^+$ T cells enhances immune pathways required for aPD-1-mediated response and results with potent anti-tumor therapeutic activity.

Shapir Itai et al., 2024, Cell *187*, 375–389
January 18, 2024 © 2023 Elsevier Inc.
https://doi.org/10.1016/j.cell.2023.12.011

CellPress

Cell

CellPress

Article

Bispecific dendritic-T cell engager potentiates anti-tumor immunity

Yuval Shapir Itai,[1,5] Oren Barboy,[1,5] Ran Salomon,[1] Akhiad Bercovich,[2] Ken Xie,[1] Eitan Winter,[1] Tamar Shami,[4] Ziv Porat,[3] Neta Erez,[4] Amos Tanay,[2] Ido Amit,[1,5,*] and Rony Dahan[1,5,6,*]

[1]Department of Systems Immunology, Weizmann Institute of Science, Rehovot 7610001, Israel
[2]Department of Computer Science and Applied Mathematics, Weizmann Institute of Science, Rehovot 7610001, Israel
[3]Flow Cytometry Unit, Life Science Core Facility, Weizmann Institute of Science, Rehovot 7610001, Israel
[4]Department of Pathology, Faculty of Medicine, Tel Aviv University, Tel Aviv 69978, Israel
[5]These authors contributed equally
[6]Lead contact
*Correspondence: ido.amit@weizmann.ac.il (I.A.), rony.dahan@weizmann.ac.il (R.D.)
https://doi.org/10.1016/j.cell.2023.12.011

SUMMARY

Immune checkpoint inhibition treatment using aPD-1 monoclonal antibodies is a promising cancer immunotherapy approach. However, its effect on tumor immunity is narrow, as most patients do not respond to the treatment or suffer from recurrence. We show that the crosstalk between conventional type I dendritic cells (cDC1) and T cells is essential for an effective aPD-1-mediated anti-tumor response. Accordingly, we developed a bispecific DC-T cell engager (BiCE), a reagent that facilitates physical interactions between PD-1$^+$ T cells and cDC1. BiCE treatment promotes the formation of active dendritic/T cell crosstalk in the tumor and tumor-draining lymph nodes. *In vivo*, single-cell and physical interacting cell analysis demonstrates the distinct and superior immune reprogramming of the tumors and tumor-draining lymph nodes treated with BiCE as compared to conventional aPD-1 treatment. By bridging immune cells, BiCE potentiates cell circuits and communication pathways needed for effective anti-tumor immunity.

INTRODUCTION

Cancer treatments have advanced significantly over the last decade, augmented by immunomodulatory therapies that enhance host anti-tumor immunity. In particular, programmed cell death protein 1 (PD-1) immune checkpoint blocking monoclonal antibodies (mAbs) have been shown to elicit durable responses in subsets of patients across various tumor types.[1] However, a majority of patients do not respond to the treatment or experience a recurrence of the disease after an initial response.[2] It is therefore essential to identify the reasons for unresponsiveness and to develop approaches to increase the potency and response rate for antibody-based immune checkpoint inhibitors.

Exhausted T cells (T_{EX}) constitute heterogeneous PD-1-expressing T cell populations characterized by their reduced ability to secrete interferon-γ (IFN-γ) and limited effector functions. While it is widely accepted that PD-1 mAbs work through reinvigorating the effector state and antitumor activity of T cells, the detailed molecular and cellular pathways leading to this outcome are incompletely understood. Progenitor exhausted cells (T_{PEX}) are a distinct PD-1$^+$ cell population that retain proliferative capabilities and undergo self-renewal to give rise to additional T_{EX} subsets cells.[3–6] The T_{PEX} cells are key players during aPD-1 immunotherapy, providing the source of the treatment-responding effector cell pool that proliferates and differentiates into effector-like T cells.[4,7]

It has been increasingly recognized that dendritic cells (DCs) are essential for effective anti-tumor immunity[8–10] and for successful aPD-1 therapy.[11–14] Of particular interest are conventional DCs, a diverse group of professional antigen-presenting cells (APCs) that, while present in low numbers within tumors and lymphoid organs, play critical roles in initiating[8,9,15] and regulating[10,16] tumor-specific adaptive and innate immunity, with specific DC subsets associated with enhanced tumor growth control and increased survival in several cancer types.[15,17–23] Most relevant are conventional type I dendritic cells (cDC1s), which are potent activators of the tumor immune response through antigen presentation to CD8$^+$ T cells[24,25] and secretion of IL-12 and which lead to the activation of CD4$^+$ T cells and their polarization toward a Th1 phenotype.[26] DC frequency in human tumors is directly correlated with a positive response to PD-1 checkpoint blockade.[19] DCs are essential for the early priming of anti-tumor T cell immunity before the induction of the T cell exhaustion program. Moreover, recent data suggest that DCs are also required during the active stage of aPD-1 administration for an effective response to the treatment.[12,13,27,28] In line with these data, T_{PEX}-DC colocalization in patients has been correlated with favorable prognosis in multiple tumor types.[29–32] Taken together, these findings

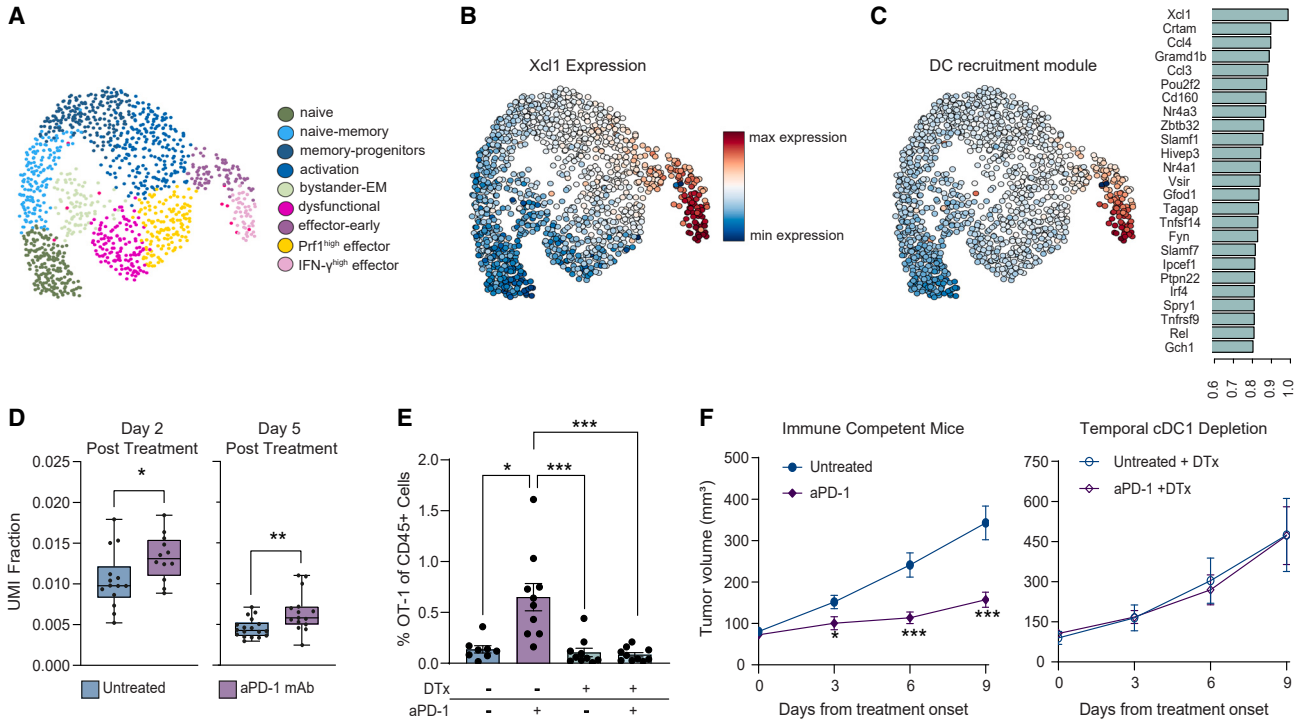

Figure 1. cDC1s mediate T cell efficacy during aPD-1 immunotherapy

(A) 2D projection of the CD8$^+$ transcriptional manifold from spleen, tumors, and dLNs of mice bearing B16-OVA and MC38 tumors. Colors annotated states of metacells.

(B) Projection of Xcl1 expression levels overlayed on the CD8$^+$ transcriptional manifold.

(C) Expression of DC recruitment gene module consisting of the 25 listed genes (right), projected on the CD8$^+$ transcriptional manifold (left). Pearson correlation of the expression of the 25 genes to the expression of Xcl1 is shown in the right bar graph.

(D) Boxplots of unique molecular identifier (UMI) fraction of the DC recruitment gene module expression between control and PD-1 mAb treated mice, at days 2 and 5 following treatment initiation. Each dot represents an individual mouse. Combined data from two independent experiments is shown.

(E) Fraction of T_{OT-1} from total live CD45$^+$ cells gated from B16-OVA tumors of Xcr1-iDTR mice. Each dot represents an individual mouse. Combined data from two independent experiments is shown.

(F) Tumor growth rate of B16-OVA tumor cells in XCR1-iDTR mice following OT-1 CD8$^+$ adoptive transfer, treated with PD-1 mAb with or without DTx injections for temporal cDC1 depletion. n = 10 mice.

Unless otherwise stated, results are presented as means ± SEM. Stars indicate a significant p value as calculated by the relevant statistical test (see methods). See also Figure S1.

underscore the importance of T cell–DC crosstalk within the tumor microenvironment (TME) to elicit effective anti-tumor immune responses.

Here, we applied single-cell transcriptional analysis of the TME to identify DC-related pathways limiting the antitumor immunity engaged by aPD-1 treatment. Based on our findings, we designed and developed a new family of bispecific antibody-based immunotherapies that engage PD-1$^+$ T cell–DC physical interactions to promote potent tumor-specific immunity.

RESULTS

cDC1s mediate T cell efficacy during aPD-1 immunotherapy

To gain insight into the molecular phenotypes that govern the crosstalk between CD8$^+$ T cells and DCs during PD-1 inhibition therapy, we profiled a dynamic transcriptional manifold of 129,147 CD8$^+$ T cells from 205 tumor-bearing mice following aPD-1 treatment, or untreated controls using single-cell RNA sequencing (scRNA-seq).[33] We tracked nine molecularly distinct CD8$^+$ T cell states *in vivo* over time in draining lymph nodes (dLN), spleen, and tumors of mice bearing MC38 colon adenocarcinoma or B16-OVA melanoma, from endogenous T cells, and adoptively transferred tumor-specific T_{OT-1} cells (Figure 1A). Through this atlas, we observed high expression of the cDC1 chemoattractant, Xcl1, in cell states (effector-early, IFN-γ^{high} effector) associated with the early stages of the tumor-specific CD8$^+$ cytotoxic response to aPD-1 therapy in the TME (Figure 1B). These Xcl1-expressing states co-expressed high levels of activation genes such as Tnfrsf9, Irf8, Il2ra, Ifng, Nfkbid, Tnf, CD40lg, Nr4a1, and Tnfsf14. Based on this observation, we derived a DC recruitment (DC-r) gene module (including genes such Crtam, Ccl4, Ccl3, and CD160) from the data, which was based on the correlation with the expression of Xcl1 in the effector-early and IFN-γ^{high} effector states of the CD8$^+$ manifold (Figures 1C and S1A).

We then wished to investigate the effect of aPD-1 administration on the expression of the DC-r gene module in tumor-specific

T cells. To this end, we utilized the B16-OVA tumor model combined with OVA-specific $CD8^+$ T_{OT-1} cell adoptive transfer following tumor inoculation, and treatment with aPD-1. We found significantly higher expression of the DC-r module in aPD1-treated mice compared to controls, both at an early and later time point following the onset of antibody treatment (Figure 1D). To further understand the role of cDC1 in mediating the effects of aPD-1 treatment, we utilized Xcr1-iDTR mice, which allow inoculation and establishment of tumors within a competent immune system followed by inducible cDC1 depletion (Figure S1B), limited to the time of the immunotherapy administration. We evaluated the effect of aPD-1 mAb therapy on the proliferation and recruitment of tumor-specific T_{OT-1} cells in the presence or absence of cDC1s and found that aPD-1 treatment led to a significant increase in the frequencies of tumor-specific $CD8^+$ cells 5 days following treatment onset, only if cDC1s were present at the time of the therapeutic mAb injections (Figure 1E). Furthermore, the significant reduction in tumor growth of aPD1-responsive MC38 (Figure S1C) and B16-OVA (Figure 1F) tumors following aPD-1 mAb monotherapy was completely lost when diphtheria toxin (DTx) was injected to the mice, resulting in almost complete depletion of cDC1 24 h before initiation of treatment. Taken together, these findings strongly support the hypothesis that the interaction of $CD8^+$ $PD\text{-}1^+$ T cells with cDC1s during the active stage of aPD-1 therapy is essential to enhance $CD8^+$ $PD\text{-}1^+$ T cell proliferation and for mediating a potent cytotoxic antitumor response.

Bispecific DC-T cell engager (BiCE)

Our findings underscore the importance of $PD\text{-}1^+$ T cell–cDC1 interactions during PD-1 inhibition therapy. Since cDC1 are a relatively rare immune population within the TME,[15] we hypothesized that the low probability of T cell–cDC1 interactions may be a limiting factor for an effective T-cell-mediated response to aPD-1 treatment. We therefore designed a bispecific antibody (bsAb) that promotes physical interactions in the tumor and tumor-draining lymph nodes between cDC1 and $PD\text{-}1^+$ T cells to facilitate anti-tumor immune activation. We refer to this reagent as a Bispecific DC-T Cell Engager (BiCE). Our BiCE was designed using a native IgG-like bispecific format, with one Fab arm that binds PD-1 and blocks its interaction with PD-L1 and a second Fab that binds the cDC1 surface marker CLEC9A (DNGR1) (Figure 2A). CLEC9A was selected due to its highly cDC1-selective expression profile in both mice and humans.[34,35] We also designed a monovalent aPD-1 bsAb with an isotype control instead of the CLEC9A binding arm (PD-1/IC) to serve as a control for PD-1 blockade without cDC1 engagement in a comparable format to that of BiCE. The Fc of BiCE was mutated to avoid interactions with Fcγ receptors (FcγR) and to prevent the engagement of Fc-effector function and unwanted depletion of the targeted cells. BiCE was produced and purified as a homogeneous heterodimer containing the anticipated binding specificity of the two constituent antibodies (Figures 2B, S2A, and S2B). BiCE displayed reduced PD-1 binding compared to its parental aPD-1 mAb (IC50 = 3.54 μg/mL and 1.50 μg/mL, respectively) as expected due to the monovalent versus bivalent PD-1 binding of the bsAb vs. the mAb formats. BiCE was able to simultaneously bind its two targets and promote dose-dependent $PD\text{-}1^+$ and $CLEC9A^+$ cell conjugates (Figures 2C and S2C). Furthermore, BiCE promoted dose-dependent T cell–DC doublet formation in mice splenocytes, indicating its effective cell bridging of the targeted cells (Figures 2D and S2D–S2F).

BiCE forms activated DC-T cell conjugates

To assess the ability of BiCE to form T–DC synapses *in vivo* at its target site, we analyzed B16F10 melanoma tumors and tumor dLNs from BiCE-injected mice at multiple timepoints (Figure 3A). We observed increased frequencies of T cell–cDC1 doublets in the dLN 24 h following PD-1/CLEC9A BiCE injection, but not after injection of aPD-1 bsAb control, a format with no cDC1-binding arm (PD-1/IC) (Figure 3B). Both the frequency of cDC1 (Figure 3C) and their fraction that forms doublets with T cells in the dLN of the BiCE-injected mice at this timepoint increased (Figure S3A), indicating that BiCE increases the proportion of T–DC physical interactions from an enlarged cDC1 pool. The observed elevation in cDC1s in the dLN is concurrent with an increase in migratory cDC1 ($CD103^+$) (Figure 3D), but not resident cDC1 ($CD103^-$) (Figure S3B). In parallel, we observed a significant decrease in total cDC1 frequency in the TME (Figure S3C) mediated by a decrease in migratory cDC1, while resident cDC1 remained unchanged (Figures 3E and S3D), suggesting increased migration of cDC1 from the TME to the tumor dLNs upon BiCE treatment. We investigated the contribution of migratory cDC1s versus resident cDC1s to T cell–cDC1 doublet composition in the dLN and found that their relative frequency within T cell–cDC1 doublets from BiCE-treated mice was significantly increased compared to migratory cDC1 frequency in cell doublets of control-treated mice (Figure 3F). This increased abundance of migratory cDC1 within the cDC1–T cell doublets is consistent with both the increased influx of migratory cDC1s to the dLN in treated mice and the heightened CLEC9A expression by migratory cDC1s relative to resident cDC1s (Figure S3E). The migration and doublet formation observed with BiCE treatment were specific to cDC1s in the tumor dLN, while BiCE treatment did not increase doublet formation in the spleen and lungs, nor did it increase cDC1 infiltration to these organs (Figure S3F). Since plasmacytoid DC (pDC) also expresses CLEC9A, although at reduced density compared to cDC1 (Figures S3G–S3I), we evaluated pDC frequency in T cell–cDC1 dLN doublets in response to BiCE treatment. In contrast to T cell–cDC1 doublets, we did not observe increased T cell–pDC doublets following the BiCE injections (Figure S3J). Thus, BiCE promotes targeted DC–T cell doublet formation in the dLNs that is mediated by the migratory cDC1 subpopulation, and is restricted to the tumor and dLN sites.

Next, we employed imaging flow cytometry to investigate whether the BiCE-mediated formation of DC-T cell contacts is a result of its direct bridging of $PD\text{-}1^+$ T cells and $CLEC9A^+$ cDC1s or a secondary event resulting from the treatment. Accordingly, tumor-bearing mice were treated with fluorescently labeled BiCE, and dLN doublets were assessed by imaging flow cytometry (Figures 3G–3I). The injected PD-1/CLEC9A BiCE were preferentially localized at the DC/T interface of interacting DC/T cells conjugates (Figure 3H), resulting in significantly higher staining intensity at the interface relative to staining by PD-1/IC (Figures 3I and S3K). BiCE localized significantly closer to the

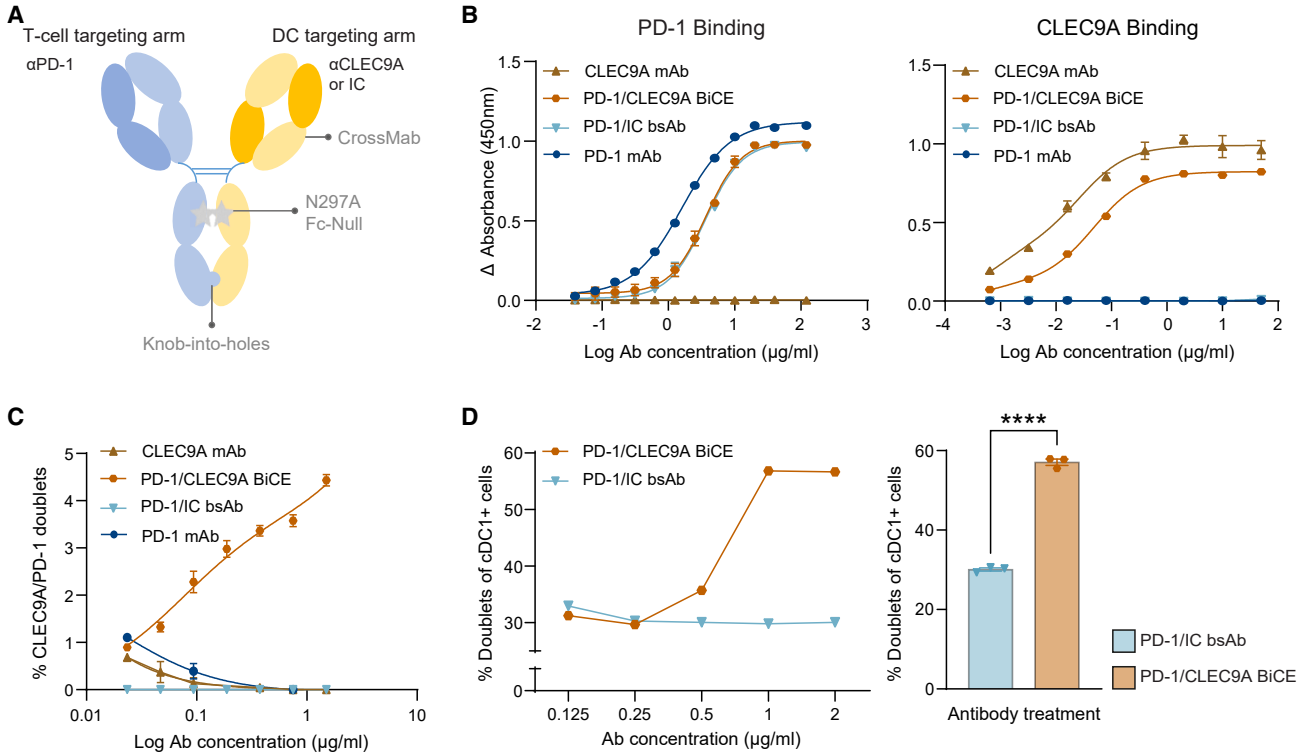

Figure 2. Design and characterization of the Bispecific DC-T Cell Engager (BiCE)

(A) Scheme showing the BiCE construct.

(B) Binding ELISA to PD-1 and CLEC9A. Dose-titration of binding of the indicated monospecific and bispecific antibodies to recombinant PD-1 and CLEC9A proteins.

(C) Cell-bridging assay of HEK293 transfected cells. A 1:1 mixture of PD-1 and CLEC9A-expressing cells were incubated with the indicated concentration of the monospecific and bispecific antibodies. The percentage of PD-1/CLEC9A pairs was quantified from live doublets.

(D) Cell-bridging assay of mouse splenocytes. $CD8^+$ T cells were isolated from naive mice and activated to express PD-1. Then, cells were incubated with whole splenocytes and the indicated concentration of bispecific antibodies. T cell/cDC1 doublets were quantified via flow cytometry. One independent experiment of three is shown.

Unless otherwise stated, results are presented as means ± SEM. Stars indicate a significant p value as calculated by the relevant statistical test. See also Figure S2.

cell membrane of $MHCII^+$ cells in T–DC doublets as compared to its more ubiquitous intracellular and membranal localization on $MHCII^+$ singlets (Figure S3L), suggesting that BiCE internalization can occur in single $MHCII^+$ cells, but such internalization is prevented when binding T cells *in trans* to form cell doublets. Altogether, our results indicate that BiCE directly enforces the physical interaction of $CLEC9A^+$ cDC1 and $PD\text{-}1^+$ T cells *in vivo* with increased numbers of cDC1 cells and DC/T conjugates in the dLN of treated mice.

To characterize the molecular phenotype of the BiCE-induced cDC1–T cell doublets, we applied 'single-cell sequencing of physically interacting cells' (PIC-seq) technology[36] on the dLN of mice treated with the PD-1/CLEC9A BiCE. We also sequenced singlets of $CD3^+$ T cells and $CD11c^+MHCII^+XCR1^+$ DCs collected from the dLN 24 h after BiCE treatment in B16F10-bearing mice. We then modeled the conjugates of $MHCII^+CD11c^+XCR1^+CD3^+$ PICs tethered *in vivo* by the BiCE molecule by inference of their T cell and dendritic cell identities. We conservatively grouped T and DC metacells based on hallmark gene expression (Figures 3J and S3M) into naive T cells (Tcf7, Lef1, Sell), activated T cells (Stat1, Nkg1, Prf1), cDC1 (Xcr1, Clec9a), and activated DC (Ccr7, CD83). Activated T cells in the physically interacting cells (PICs) were enriched in $CD8^+$ cells, while the naive T cells were enriched in $CD4^+$ cells. Notably, the PICs were characterized by a significant enrichment in the frequency of activated DC and T cells compared to non-interacting single cells (Figure 3K). To gain further insight into the molecular signature of the physically interacting DC and T cells, differential gene expression analysis was performed between the observed and expected expression derived from the null model of PIC-seq (Figure 3L). In interacting cells, we observed upregulation of the chemokine Xcl1 in T cells, as well as several genes involved in cell division and cell cycle regulation (Lgals1, Cdc20, Cenpa, and Mcm2). Altogether, dissection of the physically interacting DC and T cells induced by PD-1/CLEC9A BiCE treatment shows the preservation of a potent immune response, which results in both the activation and proliferation of T cells and the maturation of cDC1. This implies that BiCE

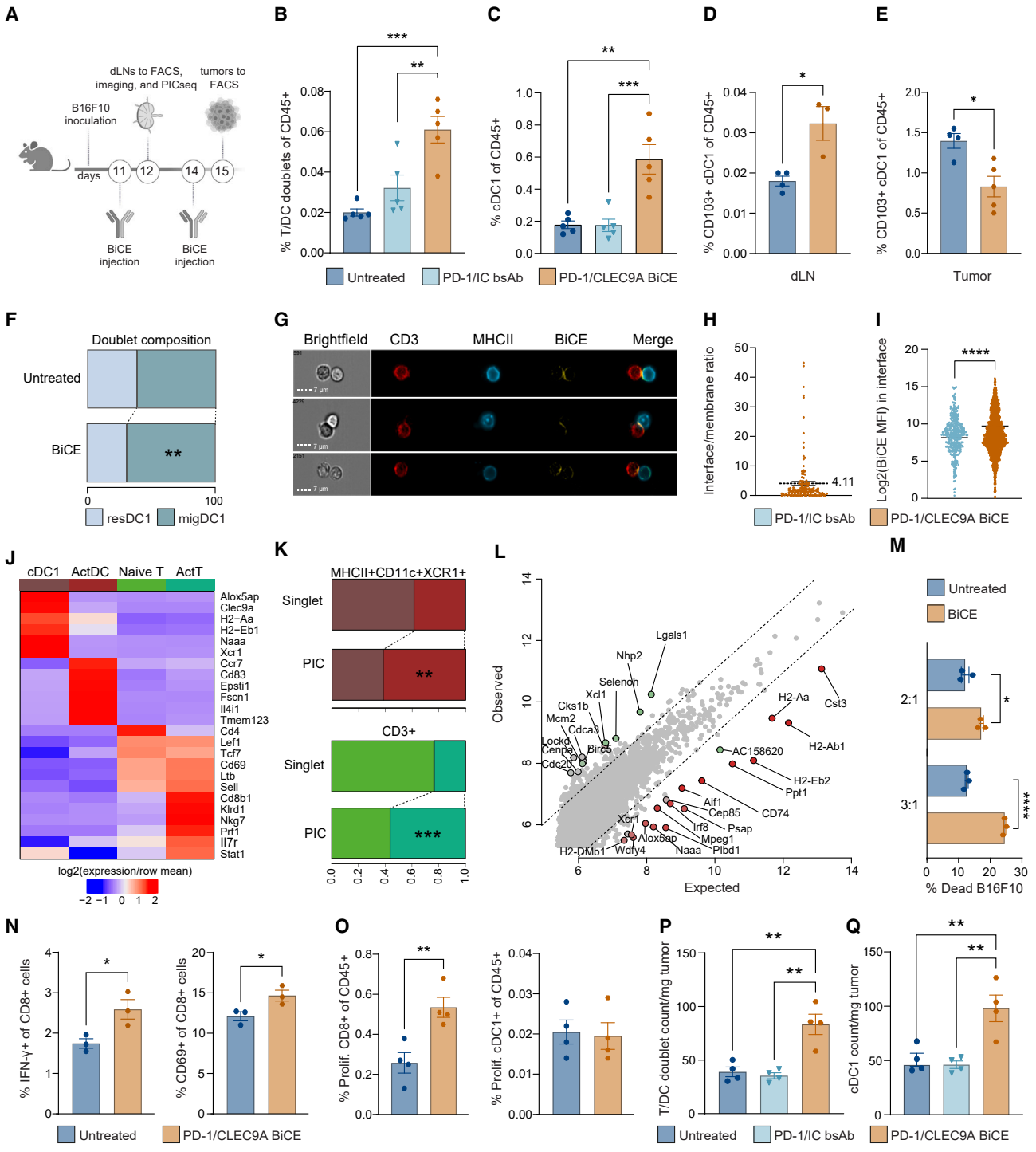

Figure 3. BiCE forms activated DC-T cell conjugates

(A) Illustration of the experimental workflow of the data presented in panels (B-Q).

(B) T–DC doublet frequencies in the tumor-draining lymph nodes of B16F10-bearing mice following the indicated treatments. Cell doublets were calculated as the percentage of CD3/cDC1 pairs from total immune cells. Each dot represents a single mouse; one independent experiment of three is shown.

(C) Frequencies of cDC1 in the tdLN quantified by flow cytometry. Each dot represents a single mouse; one independent experiment of three is shown.

(D and E) Frequency of cDC1 subsets in the dLN (D) and tumor (E), calculated by flow cytometry 24 h following BiCE injection. Each dot represents a single mouse; one independent experiment of two is shown.

(F) cDC1 subset composition of dLN T cell–DC doublets, 24 h following BiCE injection; n = 3–4 mice; one independent experiment of two is shown.

(legend continued on next page)

treatment increases the abundance of activated DC/T cell conjugates resulting in enhanced immune function.

Next, we wished to evaluate the mode of action of BiCE-mediated DC-T cell conjugate activation on antitumor immunity. We found that $CD8^+$ T cells isolated from the dLNs of B16F10 tumor-bearing mice exhibited increased IFN-γ and CD69 expression levels and enhanced tumor-killing capability following BiCE treatment (Figures 3M and 3N). We subsequently revealed a significant rise in the proliferation of $CD8^+$ T cells, but not cDC1, in BiCE-treated mice compared to the untreated group (Figure 3O). These results support a model whereby following BiCE treatment, $CD8^+$ T cells form an active synapse with cDC1 leading to enhanced $CD8^+$ T activation, proliferation, and cytotoxic activity. Furthermore, the data suggests that the increase in tumor dLN cDC1s is likely a consequence of augmented migration by $CD103^+$ cDC1s, rather than their proliferation within the dLN.

We then evaluated BiCE-mediated T–DC interactions at the tumor site by analyzing the kinetics of their doublet formation. We treated B16F10-bearing mice with PD-1/CLEC9A BiCE or control and quantified T–DC doublets in the dLN and TME over time. At the dLN, the BiCE mediated early doublet formation observed 1 day post-injection (Figure 3B), which declined over time (Figure S3N). At the TME, we observed an opposite trend to that in the dLN, wherein the T–DC doublets accumulated over this time course (Figures 3P and S3O). Interestingly, 1 day following treatment onset, we observed a small, but statistically significant, increase in T–DC doublets in the TME despite the overall decreased frequency of tumor cDC1 cells at this timepoint. This emphasizes the function of BiCE in promoting T–DC interactions independent of cDC1 frequency. Moreover, this early event of DC/T cell crosstalk induction at the tumor site may contribute to the cDC1 activation and migration to the dLN, and the sequential T cell-mediated antitumor response. After 3 days at the TME, T–DC doublet numbers were further increased ($\sim$6-fold more than day 1; Figure 3P), together with the total numbers of cDC1 (Figure 3Q). Overall, our data suggest that BiCE treatment promotes the dynamic formation of active T cell–cDC1 doublets in the dLNs and tumor, leading to proliferation and activation of cytotoxic $CD8^+$ T cells.

BiCE promotes potent antitumor activity

To test the therapeutic outcome of DC-T cell engagement by BiCE, we applied treatment protocols for established primary tumors representing three aggressive tumor models: Lewis Lung Carcinoma (LLC), B16F10 melanoma, and AT3 triple-negative breast cancer (TNBC). BiCE treatment, but not the control PD-1/IC bsAb, resulted in a significant reduction in the growth rate and volume of LLC and B16F10 tumors (Figures 4A and 4B). The AT3 model did not respond to the BiCE treatment in these settings (Figure 4C). We evaluated the effect of traditional PD-1 blockade therapy (the parental PD-1 mAb clone that was constructed into the BiCE format) in these models and found that LLC and AT3 did not respond to aPD-1 treatment, while in B16F10, a therapeutic effect was seen at a level similar to that in the BiCE (Figures S4A–S4C).

As shown above, mice bearing established AT3 tumors were found to be resistant to BiCE, PD-1/IC, and aPD-1 mAb therapy. We therefore evaluated if adjuvant aCD40 agonist therapy, a DC-targeting immunotherapy that primes the cDC1/CD8 response,[35] would enhance the antitumor effect of BiCE or aPD-1 mAb (Figure S4D). TME analysis showed an elevation in $CD8^+$ T cells and cDC1 levels in tumor dLNs, and $CD8^+$ T cells in AT3 tumors of mice treated with aCD40 mAb, in comparison to untreated controls (Figure S4E), as previously demonstrated in other tumor types.[35,37] The combination of aPD-1 and aCD40 mAbs did not have an additive effect on tumor growth control beyond the effect obtained by aCD40 mAb monotherapy. In contrast, BiCE treatment resulted in a significant reduction in the tumor size of treated mice compared to those treated with aCD40 mAb alone (Figure 4D). A similar synergistic effect was observed for the combination of BiCE and aCD40 mAb in LLC and B16F10 tumors (Figures S4F and S4G).

Thus, in these refractory primary tumors, BiCE demonstrated superior efficacy to PD-1 mAb treatment as a monotherapy for LLC and as part of aCD40 mAb combination therapy for AT3.

(G) Imaging flow cytometry of dLNs 24 h following the administration of labeled BiCE. Cells were defined based on morphology, size, and CD3 or MHCII expression. Representative images of DC/T cell doublets.
(H) Quantification of BiCE accumulation at the interface of T–DC contact relative to the rest of the cell membranes. Each dot represents a single T–DC pair; one independent experiment of two is shown.
(I) BiCE intensity at the site of DC-T cell contact calculated by quantifying the MFI of BiCE in the interface between the two cell types. Each dot represents a single T–DC pair; n = 3 mice; one independent experiment of three is shown.
(J) scRNA-seq of $CD3^+$ and $MHCII^+$ $CD11c^+$ $XCR1^+$ of a pool of 15 draining lymph nodes from mice bearing B16F10 tumors. Mean log normalized counts of selected genes across the four cell annotations (row scaled).
(K) Distribution of T cell or DC subsets in $CD3^+$ singlet T cells or $MHCII^+$ $CD11c^+$ $XCR1^+$ cDC1 singlets, vs. PIC doublets containing both cell types from 15 pooled draining lymph nodes of mice bearing B16F10 tumors. Colors are based on the annotation of T cell and DC subsets shown in J; chi-square test.
(L) PIC-seq observed gene expression levels in $CD3^+$/$MHCII^+$ $CD11c^+$ $XCR1^+$ doublets plotted against their expected levels based on scRNA-seq. Genes with observed:expected ratio >3 are highlighted, and colored by their specificity to the T cell (green) or XCR1+ (red) expected contributions (log2(fold change)) between the two background populations.
(M and N) Tumor killing assay of $CD8^+$ T cell isolated from tumor dLN of treated mice (M). The frequency of IFN-γ^+ and $CD69^+$ was calculated from $CD8^+$ T cells (N). Data shown from 4 pooled dLNs/group. Each dot represents a technical replicate; one independent experiment of two is shown.
(O) Frequency of proliferating $CD8^+$ or cDC1 cells, identified by $BrdU^+$ $Ki67^+$ cells in dLNs via flow cytometry, 24 h following treatment and BrdU injection. Each dot represents a single mouse.
(P and Q) Quantification of T–DC doublets in B16F10 tumors following BiCE treatment. The absolute number of T–DC doublets and cDC1s per mg tumor was calculated by flow cytometry. Each dot represents a single mouse; one independent experiment of three is shown.
Unless otherwise stated, results are presented as means ± SEM. Stars indicate a significant p value as calculated by the relevant statistical test. See also Figure S3.

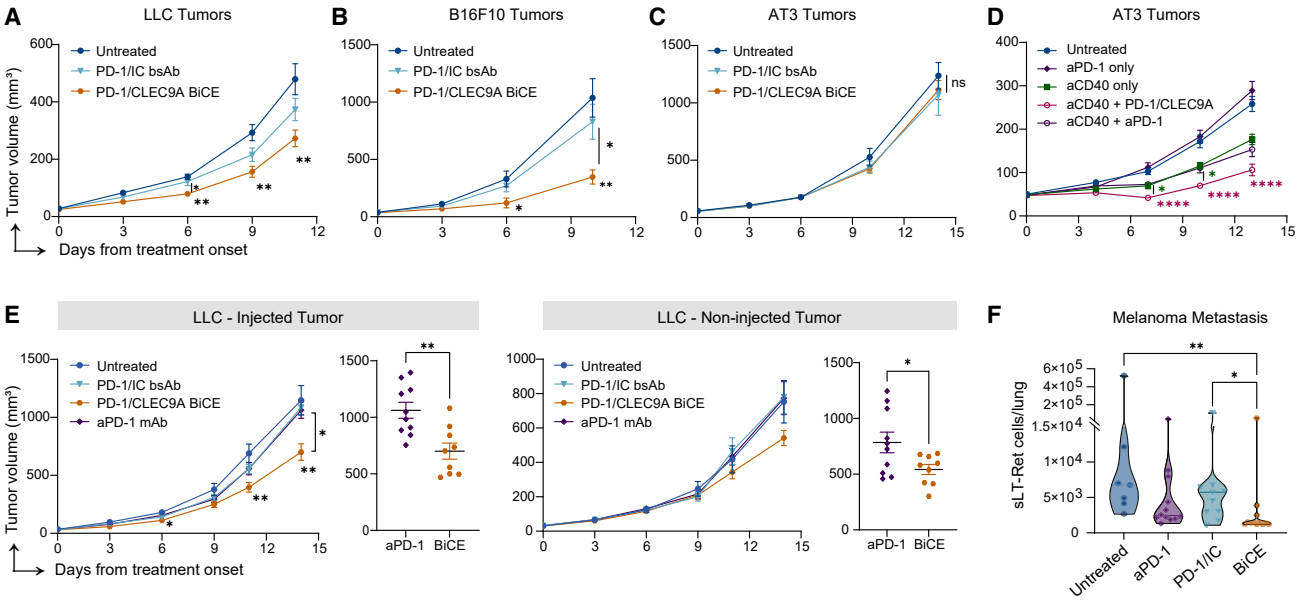

Figure 4. BiCE promotes antitumor activity

(A) Tumor growth in LLC-bearing mice was monitored following the indicated treatments. n = 10 mice; one representative experiment of three independent replicates is shown.

(B) Tumor growth in B16F10-bearing mice was monitored following the indicated treatments. n = 20 mice; one representative experiment of three independent replicates is shown.

(C) Tumor growth in AT3-bearing mice was monitored following the indicated treatments. n = 10 mice; one representative experiment of two independent replicates is shown.

(D) Tumor growth in AT3-bearing mice was monitored following treatment. n = 20 mice; one representative experiment of two replicates is shown. Green stars indicate the significance between aCD40 and aCD40+ BiCE groups, pink stars indicate the significance between untreated/aPD-1 and aCD40+BiCE groups.

(E) Tumor growth following intra-tumoral treatment of LLC tumors. Tumors were inoculated at both flanks, while tumor at only one flank was treated via intra-tumoral injection (left). n = 10 mice; results from one experiment are shown.

(F) Flow cytometry quantification of tdTomato^{+} cancer cells in lung metastases of mice injected with of sLT-Ret melanoma cells, following treatment and resection of primary tumors. Each dot represents a single mouse; results from one experiment are shown.

Unless otherwise stated, results are presented as means ± SEM. Stars indicate a significant p value as calculated by the relevant statistical test. See also Figure S4.

Similar efficacy was observed for these two reagents in the treatment of B16F10 melanoma. To explore the systemic and persistent effects of BiCE treatment, we expanded our study to encompass two additional PD-1 unresponsive clinically relevant tumor settings. First, we tested an *in situ* treatment approach for LLC tumors, utilizing mice bearing tumors at two distant sites. We treated one tumor locally by intra-tumoral injection and assessed changes in tumor growth at each location. Remarkably, BiCE treatment, but not traditional aPD-1 treatment, resulted in a robust abscopal effect, manifested by significant control of tumor volume in both the injected and distal sites (Figure 4E).

Since PD-1 immunotherapy is often applied in neoadjuvant regimes to treat patients with metastatic disease, following surgical removal of the primary tumor, we next tested BiCE treatment efficacy utilizing a model of melanoma spontaneous metastasis to evaluate the long-term effect of BiCE on lung metastatic relapse. Mice were intradermally injected with a lung tropic variant of Ret melanoma cells, sLT-Ret melanoma, labeled with tdTomato.[38] During primary tumor progression, mice were treated with BiCE, aPD-1 mAb, or PD-1/IC control, as previously described. The primary tumors were resected after completion of the treatment regime, and mice were followed for an additional 4 weeks without additional treatment before the lungs were harvested and quantified for lung metastatic burden. Notably, BiCE treatment, but not aPD-1 mAb or PD-1/IC controls, markedly reduced lung metastasis (Figure 4F).

In summary, whether used as a monotherapy or as part of a combination treatment, BiCE consistently induces a potent antitumor response and demonstrates therapeutic efficacy across multiple aggressive tumor models, including cancer types and settings that are resistant to traditional aPD-1 therapy. This efficacy extends not only to primary tumors, but also to systemic settings and inhibition of metastases.

BiCE-mediated crosstalk enhances T cell activation and proliferation in the TME

To further characterize the anti-tumor immunity facilitated by BiCE in the TME, we assessed the intracellular expression levels of IFN-γ and IL-12, key cytokines activated following DC-T cell crosstalk.[12] Notably, at 24 h following first BiCE injection, cDC1s in DC/T doublets exhibited significantly elevated IL-12 levels. However, after 3 days, IL-12 production ceased, giving way to a significant increase in IFN-γ levels in cDC1/CD8 doublets compared aPD-1 monotherapy (Figures 5A and S5A),

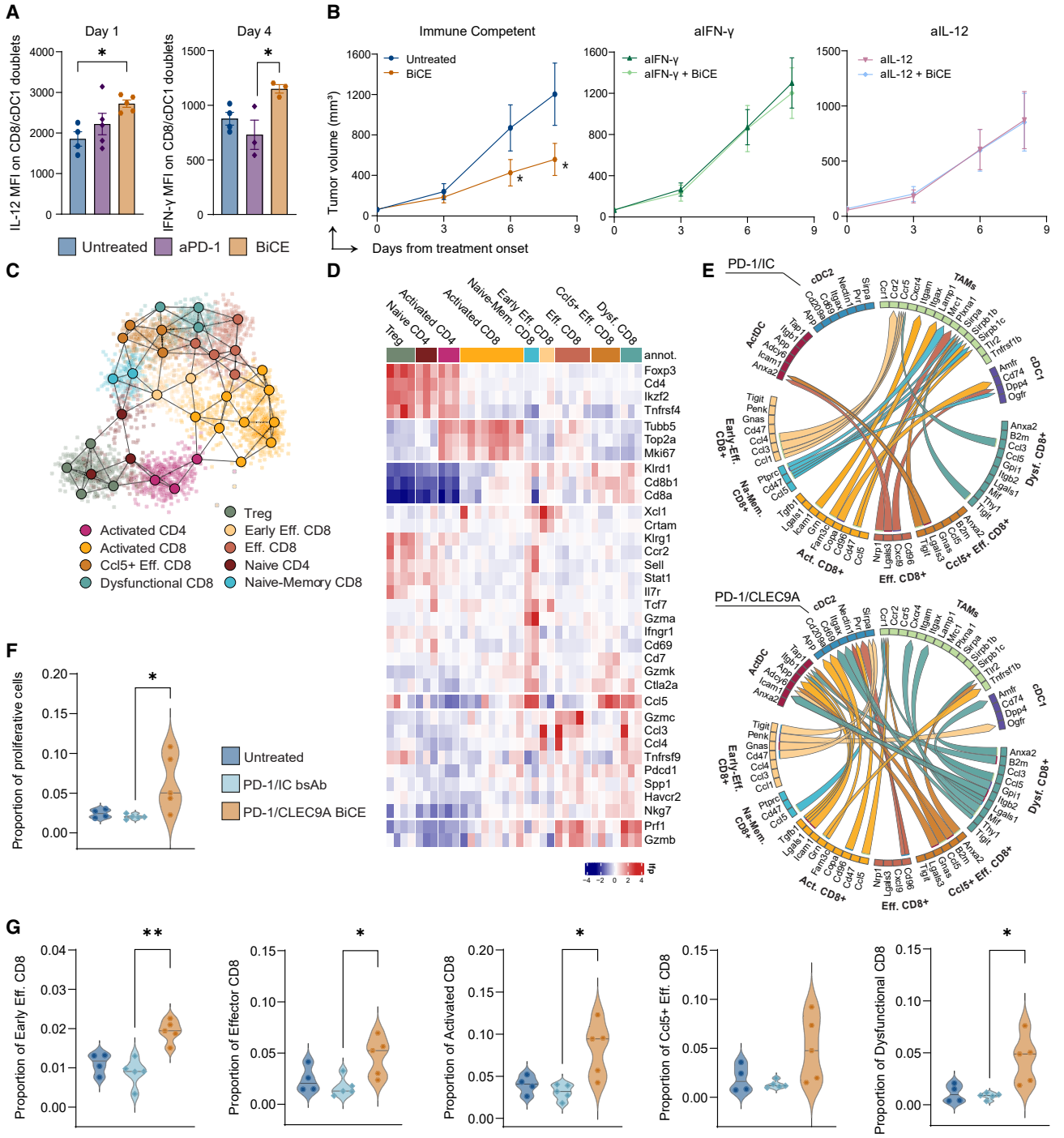

Figure 5. BiCE-mediated crosstalk enhances T cell activation and proliferation in the TME

(A) Evaluation of IL-12 levels in CD8$^+$ T cell/cDC1 tumor doublets 24 h following treatment, and of IFN-γ levels in CD8$^+$ T cell–DC tumor doublets 4 days following treatment initiation. Each dot represents a single mouse; one representative experiment of two replicates is shown.

(B) Tumor growth in B16F10-bearing mice was monitored following treatment with BiCE, neutralizing antibodies for IL-12 or IFN-γ, or their combination with BiCE. n = 9 mice; one representative experiment is shown.

(C) Two-dimensional graph projection of 35 metacells representing 3583 single-cells sorted from TCRβ$^+$ and CD45$^+$ gates from B16F10 tumors 4 days following treatment initiation.

(D) Gene expression heatmap of top selected genes from the T cell clusters.

(legend continued on next page)

indicating that BiCE-mediated interacting cells acquired the hallmark signatures of productive proinflammatory DC-T synapses. We further investigated the role of these cytokines for BiCE activity in the B16F10 tumor model by administering BiCE in the presence of IFN-γ or IL-12 neutralizing mAbs and found that both pathways were individually essential for BiCE's anti-tumor effect (Figure 5B).

Subsequently, we aimed to further explore the molecular mechanisms of the BiCE treatment. To achieve this, we conducted scRNA-seq analysis on T cells derived from B16F10 tumor-bearing mice 4 days following treatment onset. Analysis of the data using the MetaCell algorithm identified 35 metacells including diverse immune subsets isolated from the TME (Figures 5C and 5D). We focused our analysis on the T cell compartment and identified nine major T cell subpopulations based on their transcriptomic signature: naive/memory-like $CD8^+$, activated $CD8^+$, effector $CD8^+$, early-eff. $CD8^+$, $Ccl5^+$ effector $CD8^+$, dysfunctional $CD8^+$, naive $CD4^+$, activated $CD4^+$, and Tregs. Initially, to examine the ramifications of BiCE-mediated crosstalk on the TME, we conducted a ligand-receptor network analysis between $CD8^+$ subpopulations (sender cells) and DCs and TAMs (receiver cells) from the TME of mice subjected to BiCE treatment, as compared to mice treated using PD-1/IC (Figure 5E). We observed an increase in DC/T ligand-receptor interactions in the BiCE treatment group compared to PD-1/IC, where most of the elevated ligand-receptor interactions were directed toward tumor-associated macrophages (TAMs). Next, by analysis of the proportion of cells exhibiting the proliferation signature, we observed a substantial rise in proliferative T cells following the BiCE treatment (Figures 5F, S5B and S5C). Furthermore, analysis of T cell abundances revealed a consistent and significant increase in all $CD8^+$ activation and effector states (Figure 5G).

Taken together, these results show that BiCE treatment efficacy is dependent on IFN-γ and IL-12 at early stages and modulates the tumor immune response toward T–DC interactions. Consequently, this modulation results in robust $CD8^+$ activation, proliferation, and effector function within the TME.

BiCE modulates TIL phenotypes

To better understand the mode of action leading to the potent antitumor efficacy by BiCE, we characterized the treatment effect on the tumor-infiltrating lymphocyte (TIL) composition. Tumors from BiCE- and PD-1 mAb-treated mice were harvested 5 days after completion of three treatment injections. BiCE treatment of B16F10 bearing mice resulted in a significant increase in $CD8^+$ and effector $CD4^+$ T cells, and reduced T regulatory cell (Treg) frequencies (Figure S6A), leading to a significantly increased effector/regulatory ratio compared to untreated, PD1/IC and aPD-1 treated mice (Figure 6A). Of note, none of these pro-inflammatory anti-tumor effects on TIL composition were observed in B16F10 following PD-1 mAb treatment. A similar increase in the effector/regulatory ratio of BiCE-treated mice was also observed in the LLC model and in the lungs of the sLT-Ret metastatic model. In AT3 tumor-bearing mice, a significant increase in the effector/regulatory T cell ratio post-treatment was observed only when BiCE, but not aPD-1, was combined with aCD40 adjuvant therapy (Figure 6B). These data emphasize the distinct proinflammatory molecular effects of DC-T cell crosstalk induction mediated by BiCE treatment compared to PD-1 inhibition.

To further characterize the distinct molecular effects of PD-1/CLEC9A BiCE treatment as opposed to traditional aPD-1 treatment on the T cell compartment at this later stage, we conducted scRNA-seq analysis of T cells from treated B16F10 tumor-bearing mice. Tumors and dLNs were collected from control, PD-1 mAb-treated mice, and BiCE-treated mice 5 days following the last BiCE or mAb injection. This yielded in a map of 50 metacells including 4398 $TCR\beta^+$ cells sorted from the TME (Figures 6C–6H and S6B–S6E). We identified five major T cell subpopulations based on their transcriptomic signature and alignment with our previous analysis: naive/memory-like $CD8^+$, effector $CD8^+$, dysfunctional $CD8^+$, activated $CD4^+$, and Tregs. Notably, we were able to identify the three predominant $CD8^+$ T cell populations based on their expression of Pdcd1 and Tcf7: dysfunctional $Pdcd1^+$ $Tcf7^-$, early-effector $Pdcd1^+$ $Tcf7^+$, and naive/memory $Pdcd1^-$ $Tcf7^+$ (Figure 6D). Analysis of tumor T cell abundances (Figures 6F and 6G) revealed striking distinctions in the distribution of populations between the aPD-1 and the BiCE treatment groups. Specifically, we observed a significant (from 27% to 8%) decrease in the proportion of dysfunctional $CD8^+$ T cells. Moreover, we observed a significant decrease in Tregs (from 18% to 8.5% between aPD-1 and BiCE-treated mice), as well as an increase in effector $CD8^+$ T cell subpopulations compared to untreated mice following BiCE, but not PD-1 mAb treatments. Analysis of the T effector/Treg ratio revealed striking differences between the BiCE-treated group, and the PD-1 mAb and untreated groups (Figure 6H). Similar trends were observed in the dLN (Figures S6C–S6F). Thus, BiCE treatment modulates the TIL composition into a more pro-inflammatory, anti-tumoral phenotype, distinct from the effect of traditional immune checkpoint inhibition.

Finally, we wished to characterize the early events during BiCE treatment leading to the observed modulation of the TME composition. T_{PEX} play an important role in mediating the $CD8^+$ T cell response during PD-1 inhibition therapy. These $TCF1^+$ progenitor-like $CD8^+$ T cells express high levels of XCL1 and are co-localized with cDC1 in secondary lymphoid organs and the TME.[17,39,40] We analyzed TCF1 levels in BiCE-mediated cell doublets to evaluate the engagement of T_{PEX} with cDC1, 24 h and 4 days following BiCE treatment onset (Figure 6I). At 24 h, $CD8^+$ T cells in BiCE-mediated doublets in the dLN, but not in

(E) Circos plots indicating the ligand-receptor interactions between $CD8^+$ subpopulations (sender cells) and DCs and TAMs (receiver cells). The upper panel shows the upregulated ligand-receptor interactions in the PD-1/IC bsAb treatment control and the lower panel shows the PD-1/CLEC9A BiCE treatment.
(F) Proportion of proliferative cells with proliferation score $\geq$ 0.5 over $CD45^+$ gated cells. Each dot represents a single mouse.
(G) Boxplots showing the proportion of T cell clusters over the $TCR\beta^+$ gated cells among the different treatment conditions. Each dot represents a single mouse.
Unless otherwise stated, results are presented as means ± SEM. Stars indicate a significant p value as calculated by the relevant statistical test. See also Figure S5.

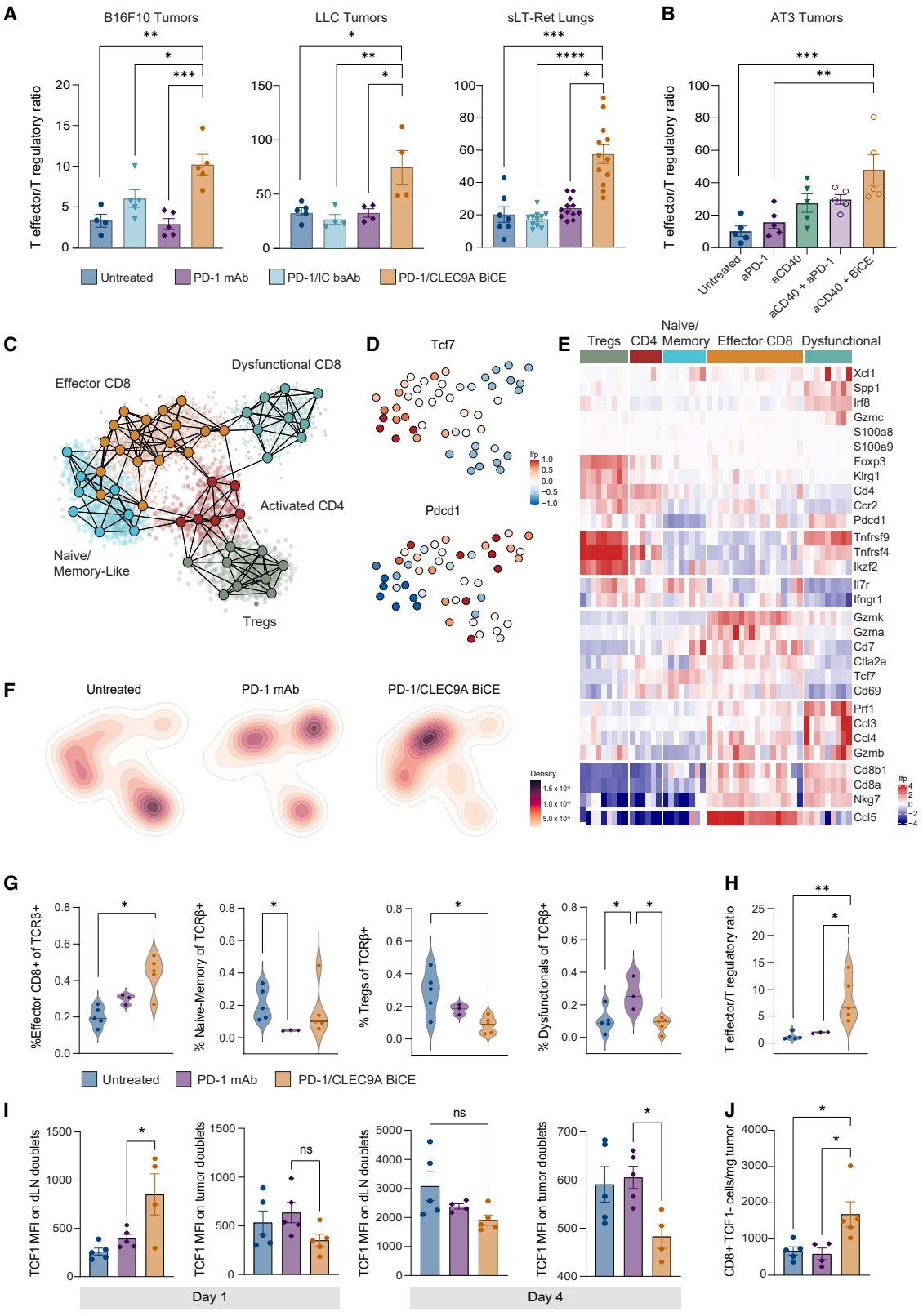

(legend on next page)

the TME, expressed significantly higher levels of TCF1 compared to T–DC doublets in PD-1 mAb-treated mice. By 4 days after treatment initiation, the early enrichment of TCF1 levels in dLN doublets was no longer observed, while in the TME, TCF1 levels in the doublets significantly decreased compared to PD-1 mAb treatment. This implies that BiCE induces doublets consisting of T_{PEX} in the dLN early after treatment onset. Activation of these T_{PEX} may lead to the rise of activated T–DC and increased $CD8^+$ proliferation in the tumor, notably of $TCF1^-$ cells (Figure 6J), leading to increased $CD8^+$ $TCF1^-$ effector-like cells ($CD44^+$ $CD62L^-$, T_{EX}, Figure S6G) at day 4 of treatment. These early events during treatment are followed by reshaping of the T cell TME approximately 1 week later, as demonstrated in Figures 6A–6H. These results highlight the unique molecular and cellular mechanisms of BiCE treatment in generating active physical contact between cDC1 and T_{PEX}, which lead to enhanced tumor-specific T cell proliferation and the remodeling of the TIL states and frequencies to favor tumor elimination.

DISCUSSION

Here, we describe a new type of antibody-based immunotherapy focused on the potentiation of the T cell–DC activation loop needed for effective tumor immunity. By analyzing the T cell transcriptional manifold during aPD-1 treatment, and by using mouse models deficient in the cDC1 subset, we demonstrate that crosstalk between a small subset of T cells and cDC1s within the TME is essential for the anti-tumor response, and is a major driving force for effective aPD-1 therapy and tumor elimination. Building on these results, we designed and developed a novel bispecific antibody that transiently engages $PD\text{-}1^+$ T cell/cDC1 physical crosstalk. BiCE treatment leads to increased numbers of interacting activated T cell–DC doublets within the tumor and the dLNs. This results in dramatic changes in the numbers and cellular states of effector immune cells in the tumor, with a mechanism distinct from that of traditional aPD-1 therapy. These cellular and molecular changes in antitumor immunity result in significant systemic and long-term tumor control in multiple aggressive tumor models. Therefore, we suggest that BiCE treatment can provide a novel immunotherapy approach, which enables the engineering of potent immune cell interactions with the potential for significant efficacy, including activity in tumors resistant to PD-1 checkpoint inhibition treatment.

The development of BiCE treatment was intended to overcome the current limitations of both DC-targeted therapies and T cell/PD-1 checkpoint inhibition, with a focus on the limited DC availability and poor interactions of T cells with DCs. This approach is supported by a significant body of recent pre-clinical and clinical data indicating that the T cell–DC axis is required for an effective response to aPD-1 treatment.[11–14,32,41] For instance, biopsies from patients treated in ICB trials suggested that effector-like $CD8^+$ T cell immunity in responders results from the formation of cellular triads of progenitor $TCF1^+$ $CD8^+$ cells with DCs and with $CXCL13^+$ $CD4^+$ T helper cells in patients with hepatocellular carcinoma (HCC),[32] or $TCF1^+$ $CD8^+$-DC doublets in melanoma[41] patients, during aPD-1 treatment. Indeed, these $TCF1^+$ stem-like $CD8^+$ cells promote optimal tumor-specific $CD8^+$ T cell priming and anti-tumor response, especially in low-antigenic settings.[42] We found that the mode of action of our BiCE similarly involves cellular interactions by promoting $TCF1^+$ $CD8^+$/cDC1 doublet formation in the dLN, which leads to the enrichment of effector-like $CD8^+$ T cells in the tumors. This suggests that BiCE treatment, compared to aPD1, has the potential to lower the $TCF1^+$ $CD8^+$ ''threshold'' or, alternatively, enhance the priming capacity required for such a response.

DC-targeted cancer immunotherapies have been extensively studied over the last two years with the ultimate goal of increasing DC abundance and function in the TME and dLNs.[43] Such DC-focused approaches include reagents that boost endogenous DC anti-tumor immunity by promoting their mobilization and activation and/or by delivering tumor antigens for cross-presentation to T cells, and DC vaccinations involving the *ex vivo* manipulation of autologous DCs and their subsequent reinfusion into patients. While much progress has been made in recent years, DC-mediated tolerance to tumors, due to non-specific targeting of the appropriate DC subsets or the tumor-associated DCs, remains a major limiting hurdle to fully

Figure 6. BiCE modulates TILs

(A) The T effector/T regulatory ratio was calculated by flow cytometry in treated B16F10 tumors, LLC tumors, and lungs of mice in the sLT-RET model, by dividing the percentages of total $CD4^+$ $FOXP3^-$ and $CD8^+$ T cells by the percentage of $CD4^+$ $FOXP3^+$ Tregs. Each dot represents a single mouse; one representative experiment of 3-2 replicates is shown for B16F10 and LLC tumors, respectively.

(B) The T effector/T regulatory ratio was calculated by flow cytometry in treated AT3 tumors. Each dot represents a single mouse, one representative experiment of two independent replicates shown.

(C) Two-dimensional graph projection of 50 metacells representing 4398 single-cells sorted from TCRβ+ gates from tumors.

(D) Projection of key marker genes onto T cell clusters.

(E) Gene expression heatmap of top selected genes from the lymphoid clusters shown in Figure S6C.

(F) Density plot of each treatment condition downsampled to 700 cells per condition in lymphoid clusters shown in Figures S6C–S6E. An equal number of cells were sampled from each individual mouse.

(G) Violin plots showing the proportion of T cell clusters over the TCRβ gated cells among the different treatment conditions. Each dot represents an individual mouse.

(H) Violin plot showing the ratio of activated $CD4^+$ T cells and effector $CD8^+$ T cells over Tregs for each treatment condition. Each dot represents an individual mouse.

(I) Barplots showing TCF1 MFI on dLN and tumor cDC1+/CD8+ doublets, 1 or 4 days following treatment initiation.

(J) Barplots showing the total number of $CD8^+$ $TCF1^-$ cells per mg tumor. For I-J, each dot represents an individual mouse; one representative experiment of three replicates is shown.

Unless otherwise stated, results are presented as means ± SEM. Stars indicate a significant p value as calculated by the relevant statistical test. See also Figure S6.

harnessing DC-based immunotherapy. The introduction of BiCE provides an advance in this direction based on its selective targeting of defined T- and dendritic-cell subsets (PD-1$^+$ and CLEC9A$^+$ cDC1, respectively) to physically promote active cancer-associated immune synapses, potentially harnessing multiple therapeutic pathways involving both cell-cell contact and secreted-mediators.

BiCE efficacy in our pre-clinical cancer models seems to involve direct activities in both the tumor site and at the tumor dLNs. While BiCE-treated mice exhibited increased cDC1 migration to the dLN, increased doublet formation, and the presence of an activated T cell and DC phenotype, T–DC interactions were observed in both the dLN and TME. We suggest that a reservoir of activated DCs remains within the TME, where their presence, along with BiCE-mediated physical interaction with CD8$^+$ T cells, provides favorable signals to the incoming T cells at a later stage, promoting effector differentiation and survival to sustain and amplify the anti-tumor response. While the described role of the TME-dLN axis in promoting T-cell-mediated immunity is largely conserved between mice and humans,[44] more recent studies indicate spatial niches within some tumor types where critical T cell–DC interactions occur, possibly bypassing the role of these interactions in the dLN.[30,32,45] Based on the characterized T cell–DC engagement by BiCE, we believe this therapy will be relevant in various clinical settings by promoting those cell interactions required for T cell responses either in the dLN or the tumor niches. Importantly, our findings suggest that BiCE treatment may be efficient as adjuvant therapy, following resection of primary tumors, to inhibit metastatic relapse.

BiCE potency can be dependent on intrinsic properties of the cDC1 or PD-1 targeting antibodies in the BiCE formats (e.g., biochemical properties such as affinity, binding epitope, and stability), or on factors related to the interaction of these antibodies and their target, e.g., conformational structural properties of the bispecific antibody while simultaneously binding each of the two proteins in-trans, and PD-1/L1 blocking activity. Considering the possible contributions of the different factors enumerated here to the potency of BiCE treatment, we suggest that our current work provides strong proof-of-concept for the BiCE approach, though modifications to the composition and properties of such bispecific reagents may further optimize the design of BiCE as potent immunotherapeutic drugs.[46]

Limitations of the study

Although this study focuses on the development of a new therapeutic approach and the mechanistic characterization of its MOA, it is important to note that all conclusions are based on pre-clinical mouse tumor models. Therefore, the potential translatability of BiCE treatment to human cancers remains largely unresolved. However, high cross-species homology and the conservation of the DC and T cell programs, along with the consequent impact of the DC/T cell axis on the outcome of anti-tumor immunity, including the response to aPD1 therapy highlight the relevance of our approach.[43,44] Our study does not address cross-species differences in the temporal dynamics within the TME, cellular composition, and the considerable heterogeneity between patients. Moreover, the BiCE approach is centered around a single major mechanism for the ICB response, while we do not address several characterized determinants dictating response versus resistance to immunotherapies, including the requirement for a pre-existing (*neo*)antigen repertoire to enable a T cell response,[47,48] and potential induction of hyperinflammation in the context of BiCE treatment. Moreover, there is still uncertainty regarding several key aspects related to the BiCE mechanism. For instance, we did not evaluate the contribution of CD4$^+$ helper T cells to the therapeutic efficacy of BiCE, nor characterize the presence of CD4$^+$ helper T cells within the BiCE-mediated doublets. It would be intriguing to evaluate whether CXCL13$^+$ CD4$^+$ T helper tumor (Tht) cells that express PD-1 are also engaged by BiCE to promote CD4$^+$ T cell–DC doublets or CD4$^+$ T cell/DC/progenitor-like CD8$^+$ triads, similar to those observed in clinical settings. The requirement for PD-1 blockade for the therapeutic effect of BiCE in addition to the cells' physical engagement is also not yet known. Lastly, our current study has yet to characterize at molecular resolution the nature of the membranal cell-contact induced by BiCE. We speculate that BiCE induces various types of DC-T cell doublets, depending on the cell state and identity of the conjugated cells. In the context of antigen specificity and cognate TCR-MHC interactions, 'classical' immune synapses between the conjugated cells may form, and could include canonical synaptic features such as induction of TCR signaling pathways, and the polarization of the centrosome and cytoskeleton. Other BiCE-induced doublets may not include these features of cytoskeletal synapses but may still function as 'synthetic' immune synapses of the engaged cells, which—when held in close proximity—may be activated by soluble mediators such as IL-12 and IFN-γ, which we show play a pivotal role in BiCE mode of action.

In this study, we combined advanced single-cell multi-omic technologies and antibody engineering to introduce a novel concept in immunotherapy: engineered physical engagement of immune cells to promote antitumor immunity. We anticipate that the extensive efforts toward characterization of cellular networks in human tumors, autoimmune and neurodegeneration cohorts will further advance our ability to develop additional types of immune engagers that promote pro-inflammatory or tissue resolution pathways by pairing cell types and states, beyond the PD-1$^+$ T cell/cDC1 axis.

STAR★METHODS

Detailed methods are provided in the online version of this paper and include the following:

- KEY RESOURCES TABLE
- RESOURCE AVAILABILITY
  - Lead contact
  - Materials availability
  - Data and code availability
- EXPERIMENTAL MODEL AND STUDY PARTICIPANT DETAILS
  - Cell lines
  - Mice
- METHOD DETAILS
  - Generation of mono- and bispecific antibodies

- Binding ELISA
- Generation of stable cell lines expressing PD-1 and CLEC9A
- Cell-based binding assay
- Mouse tumor models
- OT-1 $CD8^+$ adoptive transfer in B16-OVA bearing mice
- In-vitro splenocyte dual binding assay
- Tissue processing for flow cytometry, imaging flow cytometry, PICseq and scRNA-seq
- Flow cytometry
- Imaging flow cytometry
- BrdU proliferation assay in B16F10-bearing mice
- B16F10 killing assay in B16F10-bearing mice
- Plate-based single-cell sorting
- MARS-seq library preparation
- MARS-seq processing
- MetaCell analysis
- Analysis of the DC recruitment module
- PIC-seq summary
- MetaCell model of tdLN from B16F10 tumor-bearing mice
- PIC-seq analysis of the mouse model
- Comparing observed and expected expression
- Proliferation analysis
- Ligand-receptor analysis

- QUANTIFICATION AND STATISTICAL ANALYSIS

ACKNOWLEDGMENTS

We'd like to thank Genia Brodsky from the Scientific Illustration unit of the Weizmann Institute for her artwork. R.D. is an incumbent of the Rina Gudinski Career Development Chair, funded by the European Research Council, Israel Cancer Research Fund, Israel Science Foundation, Moross Integrated Cancer Center, Flight Attendant Medical Research Institute, Dwek Institute for Cancer Therapy Research, Teva Pharmaceuticals, Center for Immunotherapy at the Weizmann Institute of Science, David E. Stone and Sheri Hirschfield Stone 75th Anniversary Fund, Rising Tide Foundation, Miel de Botton, Garvan-Weizmann Partnership donors, and Elie Hirschfeld and Dr. Sarah Schlesinger. I.A. holds the Eden and Steven Romick Professorial Chair, and supported by the HHMI International Scholar Award, European Union (no. 101055341-TROJAN-Cell); Deutsche Forschungsgemeinschaft (DFG, German Research Foundation) –, Israel Science Foundation, Helen and Martin Kimmel awards for innovative investigation, ISF Israel Precision Medicine Program (IPMP), Dwek Institute for Cancer Therapy research grant, Moross Integrated Canceer Center grant, Ekard Institue for Cancer Diagnosis Research, Morris Kahn Institute for Human Immunology, Swiss Society Institute for Cancer Prevention research, Elsie and Marvin Dekelboum Family Foundation, Lotte and John Hecht Memorial Foundation, Schwartz Reisman Collaborative Science Program, and Betty Kahn Foundation. N.E. is supported by the Melanoma Research Alliance (award ID 826222), and the Israel Science Foundation Personalized Medicine Program (IPMP no. 3495/19).

AUTHOR CONTRIBUTIONS

Y.S.I., O.B., R.S., I.A., and R.D. conceived the project and designed the experiments. Y.S.I, R.S. and R.D. designed, generated and characterized the bispecific molecules. Y.S.I, O.B., T.S., and R.S. carried out the investigations and analyzed the data. A.B., K.X., and E.W. performed the single cell analysis, and Y.S.I. and Z.P. performed the imaging analysis. Y.S.I, O.B., I.A., and R.D. wrote the manuscript, and N.E., A.T., I.A. and R.D supervised the project. Funding was obtained by I.A. and R.D. All authors reviewed the results and approved the final version of the manuscript.

DECLARATION OF INTERESTS

The Weizmann Institute has filed a PCT patent application related to this work, on which Y.S.I., O.B., I.A., and R.D. are inventors. The patent application has been licensed to Merck Healthcare KGaA. I.A. is a member of the *Cell* advisory board.

Received: May 17, 2023
Revised: October 24, 2023
Accepted: December 5, 2023
Published: January 18, 2024

REFERENCES

1. Morad, G., Helmink, B.A., Sharma, P., and Wargo, J.A. (2021). Hallmarks of response, resistance, and toxicity to immune checkpoint blockade. Cell *184*, 5309–5337.
2. Sharma, P., Hu-Lieskovan, S., Wargo, J.A., and Ribas, A. (2017). Primary, Adaptive, and Acquired Resistance to Cancer Immunotherapy. Cell *168*, 707–723.
3. Prokhnevska, N., Cardenas, M.A., Valanparambil, R.M., Sobierajska, E., Barwick, B.G., Jansen, C., Reyes Moon, A., Gregorova, P., delBalzo, L., Greenwald, R., et al. (2023). CD8+ T cell activation in cancer comprises an initial activation phase in lymph nodes followed by effector differentiation within the tumor. Immunity *56*, 107–124.e5.
4. Im, S.J., Hashimoto, M., Gerner, M.Y., Lee, J., Kissick, H.T., Burger, M.C., Shan, Q., Hale, J.S., Lee, J., Nasti, T.H., et al. (2016). Defining CD8+ T cells that provide the proliferative burst after PD-1 therapy. Nature *537*, 417–421.
5. Utzschneider, D.T., Charmoy, M., Chennupati, V., Pousse, L., Ferreira, D.P., Calderon-Copete, S., Danilo, M., Alfei, F., Hofmann, M., Wieland, D., et al. (2016). T Cell Factor 1-Expressing Memory-like CD8(+) T Cells Sustain the Immune Response to Chronic Viral Infections. Immunity *45*, 415–427.
6. Wu, T., Ji, Y., Moseman, E.A., Xu, H.C., Manglani, M., Kirby, M., Anderson, S.M., Handon, R., Kenyon, E., Elkahloun, A., et al. (2016). The TCF1-Bcl6 axis counteracts type I interferon to repress exhaustion and maintain T cell stemness. Sci. Immunol. *1*, eaai8593.
7. Miller, B.C., Sen, D.R., Al Abosy, R., Bi, K., Virkud, Y.V., LaFleur, M.W., Yates, K.B., Lako, A., Felt, K., Naik, G.S., et al. (2019). Subsets of exhausted CD8(+) T cells differentially mediate tumor control and respond to checkpoint blockade. Nat. Immunol. *20*, 326–336.
8. Binnewies, M., Mujal, A.M., Pollack, J.L., Combes, A.J., Hardison, E.A., Barry, K.C., Tsui, J., Ruhland, M.K., Kersten, K., Abushawish, M.A., et al. (2019). Unleashing Type-2 Dendritic Cells to Drive Protective Antitumor CD4(+) T Cell Immunity. Cell *177*, 556–571.e16.
9. Hildner, K., Edelson, B.T., Purtha, W.E., Diamond, M., Matsushita, H., Kohyama, M., Calderon, B., Schraml, B.U., Unanue, E.R., Diamond, M.S., et al. (2008). Batf3 deficiency reveals a critical role for CD8alpha+ dendritic cells in cytotoxic T cell immunity. Science *322*, 1097–1100.
10. Steinman, R.M. (2012). Decisions about dendritic cells: past, present, and future. Annu. Rev. Immunol. *30*, 1–22.
11. Sánchez-Paulete, A.R., Cueto, F.J., Martínez-López, M., Labiano, S., Morales-Kastresana, A., Rodríguez-Ruiz, M.E., Jure-Kunkel, M., Azpilikueta, A., Aznar, M.A., Quetglas, J.I., et al. (2016). Cancer Immunotherapy with Immunomodulatory Anti-CD137 and Anti-PD-1 Monoclonal Antibodies Requires BATF3-Dependent Dendritic Cells. Cancer Discov. *6*, 71–79.
12. Garris, C.S., Arlauckas, S.P., Kohler, R.H., Trefny, M.P., Garren, S., Piot, C., Engblom, C., Pfirschke, C., Siwicki, M., Gungabeesoon, J., et al. (2018). Successful Anti-PD-1 Cancer Immunotherapy Requires T Cell-Dendritic Cell Crosstalk Involving the Cytokines IFN-γ and IL-12. Immunity *49*, 1148–1161.e7.
13. Ho, W.W., Gomes-Santos, I.L., Aoki, S., Datta, M., Kawaguchi, K., Talele, N.P., Roberge, S., Ren, J., Liu, H., Chen, I.X., et al. (2021). Dendritic cell

paucity in mismatch repair-proficient colorectal cancer liver metastases limits immune checkpoint blockade efficacy. Proc. Natl. Acad. Sci. USA *118*, e2105323118.

14. He, M., Roussak, K., Ma, F., Borcherding, N., Garin, V., White, M., Schutt, C., Jensen, T.I., Zhao, Y., Iberg, C.A., et al. (2023). CD5 expression by dendritic cells directs T cell immunity and sustains immunotherapy responses. Science *379*, eabg2752.
15. Broz, M.L., Binnewies, M., Boldajipour, B., Nelson, A.E., Pollack, J.L., Erle, D.J., Barczak, A., Rosenblum, M.D., Daud, A., Barber, D.L., et al. (2014). Dissecting the tumor myeloid compartment reveals rare activating antigen-presenting cells critical for T cell immunity. Cancer Cell *26*, 638–652.
16. Peng, Q., Qiu, X., Zhang, Z., Zhang, S., Zhang, Y., Liang, Y., Guo, J., Peng, H., Chen, M., Fu, Y.-X., and Tang, H. (2020). PD-L1 on dendritic cells attenuates T cell activation and regulates response to immune checkpoint blockade. Nat. Commun. *11*, 4835.
17. Chow, A., Perica, K., Klebanoff, C.A., and Wolchok, J.D. (2022). Clinical implications of T cell exhaustion for cancer immunotherapy. Nat. Rev. Clin. Oncol. *19*, 775–790.
18. Böttcher, J.P., Bonavita, E., Chakravarty, P., Blees, H., Cabeza-Cabrerizo, M., Sammicheli, S., Rogers, N.C., Sahai, E., Zelenay, S., and Reis e Sousa, C. (2018). NK Cells Stimulate Recruitment of cDC1 into the Tumor Microenvironment Promoting Cancer Immune Control. Cell *172*, 1022–1037.e14.
19. Barry, K.C., Hsu, J., Broz, M.L., Cueto, F.J., Binnewies, M., Combes, A.J., Nelson, A.E., Loo, K., Kumar, R., Rosenblum, M.D., et al. (2018). A natural killer–dendritic cell axis defines checkpoint therapy–responsive tumor microenvironments. Nat. Med. *24*, 1178–1191.
20. Schenkel, J.M., Herbst, R.H., Canner, D., Li, A., Hillman, M., Shanahan, S.-L., Gibbons, G., Smith, O.C., Kim, J.Y., Westcott, P., et al. (2021). Conventional type I dendritic cells maintain a reservoir of proliferative tumor-antigen specific TCF-1(+) CD8(+) T cells in tumor-draining lymph nodes. Immunity *54*, 2338–2353.e6.
21. Mattiuz, R., Brousse, C., Ambrosini, M., Cancel, J.-C., Bessou, G., Mussard, J., Sanlaville, A., Caux, C., Bendriss-Vermare, N., Valladeau-Guilemond, J., et al. (2021). Type 1 conventional dendritic cells and interferons are required for spontaneous CD4(+) and CD8(+) T-cell protective responses to breast cancer. Clin. Transl. Immunology *10*, e1305.
22. Ghislat, G., Cheema, A.S., Baudoin, E., Verthuy, C., Ballester, P.J., Crozat, K., Attaf, N., Dong, C., Milpied, P., Malissen, B., et al. (2021). NF-κB-dependent IRF1 activation programs cDC1 dendritic cells to drive antitumor immunity. Sci. Immunol. *6*, eabg3570.
23. Di Pilato, M., Kfuri-Rubens, R., Pruessmann, J.N., Ozga, A.J., Messemaker, M., Cadilha, B.L., Sivakumar, R., Cianciaruso, C., Warner, R.D., Marangoni, F., et al. (2021). CXCR6 positions cytotoxic T cells to receive critical survival signals in the tumor microenvironment. Cell *184*, 4512–4530.e22.
24. Haniffa, M., Shin, A., Bigley, V., McGovern, N., Teo, P., See, P., Wasan, P.S., Wang, X.N., Malinarich, F., Malleret, B., et al. (2012). Human Tissues Contain CD141 hi Cross-Presenting Dendritic Cells with Functional Homology to Mouse CD103 + Nonlymphoid Dendritic Cells. Immunity *37*, 60–73.
25. Bachem, A., Güttler, S., Hartung, E., Ebstein, F., Schaefer, M., Tannert, A., Salama, A., Movassaghi, K., Opitz, C., Mages, H.W., et al. (2010). Superior antigen cross-presentation and XCR1 expression define human CD11c+CD141+ cells as homologues of mouse CD8+ dendritic cells. J. Exp. Med. *207*, 1273–1281.
26. Soares, H., Waechter, H., Glaichenhaus, N., Mougneau, E., Yagita, H., Mizenina, O., Dudziak, D., Nussenzweig, M.C., and Steinman, R.M. (2007). A subset of dendritic cells induces CD4+ T cells to produce IFN-γ by an IL-12-independent but CD70-dependent mechanism in vivo. J. Exp. Med. *204*, 1095–1106.
27. Salmon, H., Idoyaga, J., Rahman, A., Leboeuf, M., Remark, R., Jordan, S., Casanova-Acebes, M., Khudoynazarova, M., Agudo, J., Tung, N., et al. (2016). Expansion and Activation of CD103+ Dendritic Cell Progenitors at the Tumor Site Enhances Tumor Responses to Therapeutic PD-L1 and BRAF Inhibition. Immunity *44*, 924–938.
28. Cohen, M., Giladi, A., Barboy, O., Hamon, P., Li, B., Zada, M., Gurevich-Shapiro, A., Beccaria, C.G., David, E., Maier, B.B., et al. (2022). The interaction of CD4(+) helper T cells with dendritic cells shapes the tumor microenvironment and immune checkpoint blockade response. Nat. Cancer *3*, 303–317.
29. Jansen, C.S., Prokhnevska, N., Master, V.A., Sanda, M.G., Carlisle, J.W., Bilen, M.A., Cardenas, M., Wilkinson, S., Lake, R., Sowalsky, A.G., et al. (2019). An intra-tumoral niche maintains and differentiates stem-like CD8 T cells. Nature *576*, 465–470.
30. Duraiswamy, J., Turrini, R., Minasyan, A., Barras, D., Crespo, I., Grimm, A.J., Casado, J., Genolet, R., Benedetti, F., Wicky, A., et al. (2021). Myeloid antigen-presenting cell niches sustain antitumor T cells and license PD-1 blockade via CD28 costimulation. Cancer Cell *39*, 1623–1642.e20.
31. Maier, B., Leader, A.M., Chen, S.T., Tung, N., Chang, C., LeBerichel, J., Chudnovskiy, A., Maskey, S., Walker, L., Finnigan, J.P., et al. (2020). A conserved dendritic-cell regulatory program limits antitumour immunity. Nature *580*, 257–262.
32. Magen, A., Hamon, P., Fiaschi, N., Soong, B.Y., Park, M.D., Mattiuz, R., Humblin, E., Troncoso, L., D'souza, D., Dawson, T., et al. (2023). Intratumoral dendritic cell–CD4+ T helper cell niches enable CD8+ T cell differentiation following PD-1 blockade in hepatocellular carcinoma. Nat. Med. *29*, 1389–1399.
33. Barboy, O., Bercovich, A., Li, H., Eyal-Lubling, Y., Jelinski, A., Shapir Itai, Y., Abadie, K., Zada, M., Katzenelenbogen, Y., Jaitin, D., et al. (2024). Modeling the dynamics of T cell response to immunotherapy facilitates optimization of combinatorial treatment protocols (Nat. Cancer - in press).
34. Nutt, S.L., and Chopin, M. (2020). Transcriptional Networks Driving Dendritic Cell Differentiation and Function. Immunity *52*, 942–956.
35. Salomon, R., Rotem, H., Katzenelenbogen, Y., Weiner, A., Cohen Saban, N., Feferman, T., Amit, I., and Dahan, R. (2022). Bispecific antibodies increase the therapeutic window of CD40 agonists through selective dendritic cell targeting. Nat. Cancer *3*, 287–302.
36. Giladi, A., Cohen, M., Medaglia, C., Baran, Y., Li, B., Zada, M., Bost, P., Blecher-Gonen, R., Salame, T.-M., Mayer, J.U., et al. (2020). Dissecting cellular crosstalk by sequencing physically interacting cells. Nat. Biotechnol. *38*, 629–637.
37. Garris, C.S., Wong, J.L., Ravetch, J.V., and Knorr, D.A. (2021). Dendritic cell targeting with Fc-enhanced CD40 antibody agonists induces durable antitumor immunity in humanized mouse models of bladder cancer. Sci. Transl. Med. *13*, eabd1346.
38. Doron, H., Amer, M., Ershaid, N., Blazquez, R., Shani, O., Lahav, T.G., Cohen, N., Adler, O., Hakim, Z., Pozzi, S., et al. (2019). Inflammatory Activation of Astrocytes Facilitates Melanoma Brain Tropism via the CXCL10-CXCR3 Signaling Axis. Cell Rep. *28*, 1785–1798.e6.
39. Zehn, D., Thimme, R., Lugli, E., de Almeida, G.P., and Oxenius, A. (2022). 'Stem-like' precursors are the fount to sustain persistent CD8+ T cell responses. Nat. Immunol. *23*, 836–847.
40. van der Heide, V., Humblin, E., Vaidya, A., and Kamphorst, A.O. (2022). Advancing beyond the twists and turns of T cell exhaustion in cancer. Sci. Transl. Med. *14*, eabo4997.
41. Meiser, P., Knolle, M.A., Hirschberger, A., de Almeida, G.P., Bayerl, F., Lacher, S., Pedde, A.M., Flommersfeld, S., Hönninger, J., Stark, L., et al. (2023). A distinct stimulatory cDC1 subpopulation amplifies CD8+ T cell responses in tumors for protective anti-cancer immunity. Cancer Cell *41*, 1498–1515.e10.
42. Escobar, G., Tooley, K., Oliveras, J.P., Huang, L., Cheng, H., Bookstaver, M.L., Edwards, C., Froimchuk, E., Xue, C., Mangani, D., et al. (2023). Tumor immunogenicity dictates reliance on TCF1 in CD8+ T cells for response to immunotherapy. Cancer Cell *41*, 1662–1679.e7.
43. Pittet, M.J., Di Pilato, M., Garris, C., and Mempel, T.R. (2023). Dendritic cells as shepherds of T cell immunity in cancer. Immunity *56*, 2218–2230.

44. Mellman, I., Chen, D.S., Powles, T., and Turley, S.J. (2023). The Cancer-Immunity Cycle: Indication, Genotype, and Immunotype (Preprint at Cell Press).
45. Goc, J., Germain, C., Vo-Bourgais, T.K.D., Lupo, A., Klein, C., Knockaert, S., de Chaisemartin, L., Ouakrim, H., Becht, E., Alifano, M., et al. (2014). Dendritic Cells in Tumor-Associated Tertiary Lymphoid Structures Signal a Th1 Cytotoxic Immune Contexture and License the Positive Prognostic Value of Infiltrating CD8+ T Cells. Cancer Res. *74*, 705–715.
46. Labrijn, A.F., Janmaat, M.L., Reichert, J.M., and Parren, P.W.H.I. (2019). Bispecific Antibodies: A Mechanistic Review of the Pipeline (Preprint at Nature Publishing Group).
47. Hugo, W., Zaretsky, J.M., Sun, L., Song, C., Moreno, B.H., Hu-Lieskovan, S., Berent-Maoz, B., Pang, J., Chmielowski, B., Cherry, G., et al. (2016). Genomic and Transcriptomic Features of Response to Anti-PD-1 Therapy in Metastatic Melanoma. Cell *165*, 35–44.
48. Samstein, R.M., Lee, C.H., Shoushtari, A.N., Hellmann, M.D., Shen, R., Janjigian, Y.Y., Barron, D.A., Zehir, A., Jordan, E.J., Omuro, A., et al. (2019). Tumor mutational load predicts survival after immunotherapy across multiple cancer types. Nat. Genet. *51*, 202–206.
49. Jaitin, D.A., Kenigsberg, E., Keren-Shaul, H., Elefant, N., Paul, F., Zaretsky, I., Mildner, A., Cohen, N., Jung, S., Tanay, A., et al. (2014). Massively parallel single-cell RNA-seq for marker-free decomposition of tissues into cell types. Science *343*, 776–779.
50. Keren-Shaul, H., Kenigsberg, E., Jaitin, D.A., David, E., Paul, F., Tanay, A., and Amit, I. (2019). MARS-seq2.0: an experimental and analytical pipeline for indexed sorting combined with single-cell RNA sequencing. Nat. Protoc. *14*, 1841–1862.
51. Baran, Y., Bercovich, A., Sebe-Pedros, A., Lubling, Y., Giladi, A., Chomsky, E., Meir, Z., Hoichman, M., Lifshitz, A., and Tanay, A. (2019). MetaCell: Analysis of single-cell RNA-seq data using K-nn graph partitions. Genome Biol. *20*, 206.
52. Ben-Kiki, O., Bercovich, A., Lifshitz, A., and Tanay, A. (2022). Metacell-2: a divide-and-conquer metacell algorithm for scalable scRNA-seq analysis. Genome Biol. *23*, 100.
53. Buch, T., Heppner, F.L., Tertilt, C., Heinen, T.J.A.J., Kremer, M., Wunderlich, F.T., Jung, S., and Waisman, A. (2005). A Cre-inducible diphtheria toxin receptor mediates cell lineage ablation after toxin administration. Nat. Methods *2*, 419–426.
54. Wohn, C., Le Guen, V., Voluzan, O., Fiore, F., Henri, S., and Malissen, B. (2020). Absence of MHC Class II on cDC1 Dendritic Cells Triggers Fatal Autoimmunity to a Cross-Presented Self-Antigen.
55. Dahan, R., Sega, E., Engelhardt, J., Selby, M., Korman, A.J., and Ravetch, J.V. (2015). FcγRs Modulate the Anti-tumor Activity of Antibodies Targeting the PD-1/PD-L1 Axis. Cancer Cell *28*, 285–295.
56. Schaefer, W., Regula, J.T., Bähner, M., Schanzer, J., Croasdale, R., Dürr, H., Gassner, C., Georges, G., Kettenberger, H., Imhof-Jung, S., et al. (2011). Immunoglobulin domain crossover as a generic approach for the production of bispecific IgG antibodies. Proc. Natl. Acad. Sci. USA *108*, 11187–11192.
57. Merchant, A.M., Zhu, Z., Yuan, J.Q., Goddard, A., Adams, C.W., Presta, L.G., and Carter, P. (1998). An efficient route to human bispecific IgG. Nat. Biotech. *16*, 677–681.
58. Browaeys, R., Gilis, J., Sang-Aram, C., Bleser, P.D., Hoste, L., Tavernier, S., Lambrechts, D., Seurinck, R., and Saeys, Y. (2023). MultiNicheNet: a flexible framework for differential cell-cell communication analysis from multi-sample multi-condition single-cell transcriptomics data. Preprint at. biorxiv format. 2023.06.13.544751

STAR★METHODS

KEY RESOURCES TABLE

REAGENT or RESOURCE	SOURCE	IDENTIFIER
Antibodies		
Anti-Mouse PD-1/CLEC9A BiCE (RMP1-14/10B4)	In-house	N/A
Anti-Mouse PD-1/IC bsAb (RMP1-14/Synagis)	In-house	N/A
Anti-Mouse PD-1 (RMP1-14)	In-house	N/A
Anti-Mouse CLEC9A (10B4)	In-house	N/A
Anti-Mouse CD40 (clone FGK4.5)	BioXcell	Cat# BE0016-2; RRID: AB_1107647
Anti-Mouse IFN-γ (clone XMG1.2)	BioXcell	Cat# BE0055; RRID: AB_1107694
Anti-Mouse IL-12 p40 (clone 17.8)	BioXcell	Cat# BE0051; RRID: AB_1107698
Anti-Mouse FITC-conjugated CD45 (clone 30-F11)	eBioscience	Cat#11-0451-82; RRID: AB_465050
Anti-Mouse BV650-conjugated CD45 (clone 30-F11)	BioLegend	Cat#103151; RRID: AB_ 2565884
Anti-Mouse APC/Cy7-conjugated CD45 (clone 30-F11)	BioLegend	Cat#103115; RRID: AB_312980
Anti-Mouse PE-conjugated TCR β chain (clone H57-597)	BioLegend	Cat#109207; RRID: AB_313430
Anti-Mouse FITC-conjugated TCR β chain (clone H57-597)	BioLegend	Cat#109205; RRID: AB_313428
Anti-Mouse BV650-conjugated CD11b (clone M1/70)	BioLegend	Cat#101239; RRID: AB_11125575
Anti-Mouse SB702-conjugated CD8 (clone 53–6.7)	eBioscience	Cat#67-0081-82; RRID:AB_2662351
Anti-Mouse FITC-conjugated CD8 (clone 53–6.7)	BioLegend	Cat#100705; RRID: AB_312744
Anti-Mouse PE/Dazzle-conjugated CD11b (clone M1/70)	BioLegend	Cat#101256; RRID: AB_2563648
Anti-Mouse BV421-conjugated CD3 (clone 17A2)	BioLegend	Cat#100228; RRID: AB_2562553
Anti-Mouse FITC-conjugated CD3 (clone 17A2)	BioLegend	Cat#100204; RRID: AB_312661
Anti-Mouse AF700-conjugated CD8a (clone 53–6.7)	BioLegend	Cat#100730; RRID: AB_493703
Anti-Mouse APC/Cy7-conjugated CD8 (clone 53–6.7)	BioLegend	Cat#100714; RRID: AB_312753
Anti-Mouse PE-conjugated TCF1 (clone S33-966)	BD biosciences	Cat#564217; RRID: AB_2687845
Anti-Mouse BV510-conjugated CD44 (clone IM7)	BioLegend	Cat#103044; RRID: AB_2650923
Anti-Mouse FITC-conjugated CD62L (clone MEL14)	BioLegend	Cat#104406; RRID: AB_313093
Anti-Mouse AF647-conjugated FOXP3 (clone MF-14)	BioLegend	Cat#126408; RRID: AB_1089115
Anti-Mouse APC/Cy7-conjugated CD19 (clone 1D3)	BioLegend	Cat#152412; RRID: AB_2922473
Anti-Mouse APC/Cy7-conjugated F4/80 (clone BM6)	BioLegend	Cat#123117; RRID: AB_893489
Anti-Mouse APC-conjugated CD11c (clone N418)	BioLegend	Cat#117309; RRID: AB_313778
Anti-Mouse AF700-conjugated CD11c (clone N418)	BioLegend	Cat#117319; RRID: AB_528735
Anti-Mouse PE/Cy7-conjugated CD172a (SIRPa) (clone P84)	BioLegend	Cat#144007; RRID: AB_2563545
Anti-Mouse APC/Cy7-conjugated MHCII (clone M5/114.15.2)	BioLegend	Cat#107627; RRID: AB_1659252
Anti-Mouse BV510-conjugated MHCII (clone M5/11415.2)	BioLegend	Cat#107635; RRID: AB_2561397
Anti-Mouse APC-conjugated XCR1 (clone ZET)	BioLegend	Cat#148205; RRID: AB_2563931
Anti-Mouse PerCP/Cy5.5-conjugated XCR1 (clone ZET)	BioLegend	Cat#148208; RRID: AB_2564364
Anti-Mouse PB-conjugated CD4 (clone GK1.5)	BioLegend	Cat#100427; RRID: AB_493646
Anti-Mouse PE-conjugated CD103 (clone W19396D)	BioLegend	Cat#110903; RRID: AB_2927994
Anti-Mouse APC-conjugated CD103 (clone W19396D)	BioLegend	Cat#110906; RRID: AB_2927988
Anti-Mouse BUV615-conjugated CD3 (clone 17A2)	BD biosciences	Cat#751418; RRID: AB_2875417
Anti-Mouse APC-conjugated CD19 (clone 6D5)	BioLegend	Cat#115529; RRID: AB_830706
Anti-Mouse PerCP/Cy5.5-conjugated Ly6c (clone HK1.4)	BioLegend	Cat#128011; RRID: AB_1659242
Anti-Mouse BV711-conjugated CD25 (clone PC61)	BioLegend	Cat#102049; RRID: AB_2564130
Anti-Mouse PE/Cy7-conjugated CD366 (TIM3) (clone RMT3-23)	eBioscience	Cat#25-5870-82; RRID: AB_2573483
Anti-Mouse AF700-conjugated CD62L (clone MEL-14)	BioLegend	Cat#104426; RRID: AB_493719

(*Continued on next page*)

Continued

REAGENT or RESOURCE	SOURCE	IDENTIFIER
Anti-Mouse BV510-conjugated CD279 (PD-1) (clone 29F.1A12)	BioLegend	Cat#135241; RRID: AB_2715761
Anti-Mouse PE-conjugated IFN-γ (clone XMG1.2)	BioLegend	Cat#505808; RRID: AB_315402
Anti-Mouse APC-conjugated IL-12 (clone C15.6)	BioLegend	Cat#505206; RRID: AB_315370
Anti-Mouse 488-conjugated ICAM-1 (clone YN1/1.7.4)	BioLegend	Cat#116112; RRID: AB_493493
Anti-Mouse PE-conjugated LFA-1 (M17/4) (clone M17/4)	BioLegend	Cat#101107; RRID: AB_312780
Anti-Mouse APC-conjugated CD69 (clone H1.2F3)	BioLegend	Cat#104514; RRID: AB_492843
Anti-Mouse APC-conjugated Ki67 (clone 16A8)	BioLegend	Cat#652406; RRID: AB_2561930
Purified anti-mouse CD16/32 Antibody (clone 93)	BioLegend	Cat#101301; RRID: AB_312801
PE AffiniPure F(ab')$_2$ Fragment Goat Anti-Human IgG	Jackson ImmunoResearch	Cat#109-116-170; RRID: AB_2337681
Chemicals, Peptides, Enzymes and Recombinant Proteins		
Recombinant Mouse PD-1	Sino Biological	Cat#50124-M08H
Recombinant Mouse CLEC9A	R&D Systems	Cat#6776CL050
Recombinant Mouse IL-15	PeproTech	Cat#210-15
Recombinant Mouse IL-7	PeproTech	Cat#210-07
OVA (257–264) peptide	Anaspec	Cat# S-60193
Recombinant murine IL-2	PeproTech	Cat#212-12
Streptavidin-Horseradish Peroxidase, SAv-HRP	BioLegend	Cat#405210
Albumin Bovine, Fraction V	MP-Biomedicals	Cat#9048-46-8
Collagenase IV	Worthington	Cat#LS004188
DNase I	Sigma-Aldrich	Cat#11284932001
Liberase TL	Roche	Cat#05401020001
Diphtheria Toxin	Sigma	Cat#D0564
Red blood lysis buffer	Sigma-Aldrich	Cat#R7757
EDTA	Sigma-Aldrich	Cat#03690
HBSS	ThermoFisher	Cat#14175095
HEPES 1M	ThermoFisher	Cat#15630080
DMEM	ThermoFisher	Cat#11965084
RPMI 1640 Medium	ThermoFisher	Cat#11875093
B-2-mercaptoethanol	Sigma	Cat#M6250
LIVE/DEAD™ Fixable Blue Dead Cell Stain Kit	Invitrogen	Cat#L23105
LIVE/DEAD™ Fixable Violet Dead Cell Stain Kit	Invitrogen	Cat#L34955
Zombie NIR™ Fixable Viability Kit	BioLegend	Cat#423105
DAPI (4′,6-Diamidino-2-Phenylindole, Dilactate)	BioLegend	Cat#422801
CountBright™ Absolute Counting Beads	ThermoFisher	Cat#C36950
Alexa Fluor™ 594 Phalloidin	Invitrogen	Cat#A12381
Protein G Sepharose 4 Fast Flow resin	Cytiva	Cat#17061805
Critical Commercial Assays		
CD3/CD28 T cell Activation/Expansion Kit	Milteny Biotech	Cat#130-093-627
CD8a microbeads	Milteny Biotech	Cat#130-095-236
Mouse CD8$^+$ T cell Isolation Kit	StemCell	Cat#19853
ExpiFectamine 293 Transfection Kit	Gibco	Cat#A14525
True-Nuclear™ Transcription Factor Buffer Set	BioLegend	Cat#424401
SAIVI™ Alexa Fluor™ 647 Antibody Labeling Kit	Invitrogen	Cat#S30044
Phase-Flow™ FITC BrdU Kit (clone 3D4)	BioLegend	Cat#370704
Deposited Data		
CD8$^+$ dynamic transcriptional manifold	Barboy et al., 2023[33]	GEO: GSE249630
Raw data files for single-cell RNA-seq	NCBI Gene Expression Omnibus	GEO: GSE249283

(*Continued on next page*)

Continued

REAGENT or RESOURCE	SOURCE	IDENTIFIER
Experimental Models: Organisms/Strains		
Mouse: C57BL/6JOlaHsd	Envigo	N/A
Mouse: OTI, C57BL/6-Tg(TcraTcrb)1100Mjb/J	Weizmann Institute of Science, provided by N. Friedman	N/A
Mouse: XCR1-cre-mTFP	Center d'Immunologie de Marseille Luminy, provided by B. Malissen	N/A
Mouse: XCR1-iDTR	In-house	N/A
Experimental Models: Cell Lines		
Cancer Cell Line: B16F10	ATCC	Cat# CRL-6475
Cancer Cell Line: B16-OVA	Rockefeller University	N/A
Cancer Cell Line: AT3-GFP	Hebrew University	N/A
Cancer Cell Line: L/2 (LLC1)	ATCC	Cat# CRL-1642
Cancer Cell Line: sLT-Ret-td	Tel Aviv University, provided by N. Erez	N/A
Expi293 Cells	ThermoFisher	Cat# A14527
Software and Algorithms		
MATLAB	Math Works	http://www.mathworks.com/
R 3.5.0	The R Foundation	http://www.r-project.org/
GraphPad Prism Version 9	Prism	RRID: SCR_002798
FlowJo Software Version 10.6.2	FlowJo, LLC	RRID: SCR_008520
FACSDiva 7	BD Biosciences	N/A
Other		
MARS-seq reagents	Jaitin et al., 2014[49] Keren-Shaul et al.[50]	N/A
MetaCell source code	Baran et al.[51] Ben-Kiki et al.[52]	https://github.com/tanaylab/metacell

RESOURCE AVAILABILITY

Lead contact

Further information and requests for resources and reagents should be directed to and will be fulfilled by the lead contact, Rony Dahan (rony.dahan@weizmann.ac.il).

Materials availability

Correspondence and requests for materials should be addressed to Ido Amit and Rony Dahan. All biological materials can be obtained from the corresponding authors following reasonable request.

Data and code availability

scRNA-seq data that support our findings have been deposited in the Gene Expression Omnibus and will be publicly available as of the date of publication. Accession numbers are listed in the key resources table. MetaCell source code can be found at https://github.com/tanaylab/metacell and is publicly available as of the date of publication. This paper analyzes existing, publicly available data. These accession numbers for the datasets are listed in the key resources table. Any additional information required to re-analyze the data reported in this paper is available from the lead contact upon request.

EXPERIMENTAL MODEL AND STUDY PARTICIPANT DETAILS

Cell lines

Tumor cell lines were maintained in a humidified incubator at 37°C and 5% CO_2, and cultured in complete RPMI medium containing 25 mM HEPES, 1% L-Glutamine, 10% FBS, 1% Pen Strep, 1% Non-Essential Amino acids, and 1% Pyruvate. For *in vitro* experiments, cell medium was supplemented with 0.05mM β-2-mercaptoethanol (Sigma).

Mice

All mouse experiments were performed in the Weizmann Institute of Science or Tel Aviv University specific-pathogen free facility. All animal studies were approved by the Institutional Animal Care and Use Committee of the Weizmann Institute of Science under license numbers: 06810821-2 and 06790821-2, or by the Tel Aviv University Institutional Animal Care and Use Committee. C57BL/6 mice were purchased from Envigo. Xcr1-iDTR mice were generated by crossing Rosa-lox-stop-lox-iDTR mice[53] (kindly provided by S. Jung) and Xcr1-Cre-mTFP[54] (kindly provided by B. Malissen) in our facility. TCR-transgenic OT-I mice harboring OVA-specific $CD8^+$ T cells (CD45.1) were a kind donation from the laboratory of the late Professor N. Friedman of the Weizmann Institute of Science, and maintained in our facility. Animals of both sexes were used between the ages of 8–10 weeks at the beginning of the experiment, randomized, and assigned to experimental groups.

METHOD DETAILS

Generation of mono- and bispecific antibodies

The sequence of the anti-mouse PD-1 antibody, clone RMP1-14 was obtained from Jeffery Ravetch.[55] The sequence of anti-mouse CLEC9A antibody, clone 10B4, was obtained based on patent US20130273150A. The PD-1/IC construct utilizes the sequence of the commercially available Synagis mAb (targeting RSV, an antigen not present in our experimental settings) instead of the cDC1 binding arm. The variable heavy and light regions of these antibodies were synthesized based on their published sequences (Syntezza) and cloned into mammalian expression vectors with mono human IgG1 or human kappa Fc backbones or into bispecific vectors.[56,57] To generate BiCE, the parental DC targeting arm was expressed in the CrossMab format (CH1-CL swapping), while for the PD-1 targeting arm, the wild-type sequence was maintained. For heavy chain heterodimerization, the following point mutations were introduced in the CH3 domain: Y349C/T366S/L368A/Y407V of the DC targeting arm; S354C/T366W of the PD-1 targeting arm. For the generation of the Fc-domain variant (N297A) of human IgG1, site-directed mutagenesis using specific primers was performed by PCR (Agilent Technologies) according to the manufacturer's instructions. Mutated plasmid sequences were validated by direct sequencing (Life Science Core Facility, Weizmann Institute of Science). Antibody heavy and light chain expression vectors were transiently transfected into Expi293 cells (ThermoFisher). The secreted antibodies in the supernatant were purified by protein G Sepharose 4 Fast Flow (GE Healthcare). Purified antibodies were dialyzed in PBS and sterile filtered (0.22 μm). Purity was assessed by SDS-PAGE and Coomassie staining, and was estimated to be >90%. Size exclusion chromatography (SEC) was performed using a Superose 6 Increase 10/300GL column (GE Healthcare) on an Äkta Pure 25 FPLC system.

Binding ELISA

Binding specificity and affinity of mono and bispecific Abs were determined by ELISA using recombinant mouse PD-1 (Sino Biological) and mouse CLEC9A (R&D Systems). ELISA plates (Nunc) were coated overnight at 4°C with recombinant extracellular domain of mouse PD-1 or mouse CLEC9A (1 μg ml–1). All subsequent steps were performed at room temperature. After washing, the plates were blocked for 1 h with 1xPBS with 2% BSA, and were subsequently incubated for 1 h with serially diluted IgGs (1:5 consecutive dilutions in 1xPBS with 2% BSA). For dual binding ELISA assay, plates were incubated for 1 h with 1 μg/mL biotinylated mouse PD-1 (Sino Biological). After washing, plates were incubated for 1 h with horseradish peroxidase-conjugated anti-human IgG (Jackson ImmunoResearch) or with horseradish peroxidase-conjugated Streptavidin (BioLegend). Detection was performed using a one component substrate solution (TMB), and reactions stopped with the addition of 0.18 M sulfuric acid. Absorbance at 450 nm was immediately recorded using a SpectraMax Plus spectrophotometer (Molecular Devices), and background absorbance was subtracted from negative control samples. To determine the IC50 of the antibodies, absolute IC50 was calculated using GraphPad PRISM software as recommended (GraphPad Software).

Generation of stable cell lines expressing PD-1 and CLEC9A

HEK293 cells at 70% confluence were transfected in 6-well cell culture plates (Corning) with 3 μg of pcDNA3.1-PD-1 or pcDNA-CLEC9A expression vector (Genescript) or empty vector (pcDNA 3.1) using Lipofectamine 2000 (Invitrogen) following the manufacturer's recommended procedure. After transfection, stable cell lines were established after G418 selection (800 μg/mL) for 14 days, and target expression was evaluated via FACS. Stable cell lines were cultured in DMEM supplemented with 10% FBS, 800 μg/mL G418, 1% Pen Strep (Gibco). Cultures were maintained in a humidified incubator at 37°C and 5% CO_2.

Cell-based binding assay

Single cell suspensions were prepared from transfected HEK293 cells, described above. For surface staining, cells were plated in U-shaped 96-well plates (ThermoFisher) at a concentration of 0.2-1x10^6 cells in 100 μL PBS. Cells were first stained with LIVE/DEAD Fixable blue dead cell stain (ThermoFisher) followed by two washes with PBS. Standard binding titration assay of mAbs and BiCE was performed for 30 min on ice. Cells were washed twice with FACS buffer, resuspended in 150 μL FACS buffer, and analyzed by flow cytometry. For dual-binding FACS assay, doublet engagement was assessed between HEK293 cells expressing each of the target proteins. Each cell type was stained with CFSE or CellTrace according to the manufacturer's protocol (ThermoFisher). A 1:1 mix of overexpressing cells stained with CFSE or CellTrace was used in a standard binding titration assay

of the BiCE for 30 min on ice. Cells were washed twice with FACS buffer, resuspended in 150 μL FACS buffer, and analyzed by flow cytometry. The percentage of CFSE/CellTrace pairs was quantified from live doublets.

Mouse tumor models

Tumor cell lines were maintained in a humidified incubator at 37°C and 5% CO_2, and cultured in complete RPMI medium containing 25 mM HEPES, 1% L-Glutamine, 10% FBS, 1% Pen Strep, 1% Non-Essential Amino acids, and 1% Pyruvate. Cells were routinely tested for mycoplasma. Tumor volume was calculated using the formula ($L2^2$*L1)/2, where L1 is the longest diameter and L2 is the shortest diameter.

B16F10 ($4x10^5$), LLC ($1x10^6$) and B16-OVA ($2x10^6$) were implanted subcutaneously on the right flank of mice, and tumor volumes were measured every 2–3 days with an electronic caliper by a researcher blinded to their treatment group. AT3 TNBC ($1x10^6$ cells in 1:1 Matrigel, Corning) were implanted to the right mammary fat pad. When tumor volume reached approximately 50 mm^3, (generally 7 to 11 days after tumor inoculation), mice were randomized by tumor size (day 0), and treated by intraperitoneal injection of PD-1 mAb (200μg), CD40 mAb (100μg, clone FGK4.5, BioXcell), or bsAbs (500μg) at days 0, 3, 6. In experiments where mice were initially primed with aCD40, CD40 mAb was injected on days 0 and 3, and PD-1 mAb or bsAbs were injected on days 4, 7, and 10. BiCE dosing was determined based on its relative PD-1 binding vs. that of its parental PD-1 mAb (2.5-fold differences in their IC50s) to allow similar PD-1 binding by the two antibody platforms. Mice were monitored for 8–20 days after treatment initiation, or until a tumor volume of 1500 mm^3 was reached.

For cytokine blocking experiments, mice were injected IP with 500μg anti-IFNγ (clone XMG1.2, BioXcell) or anti-IL-12p40 (clone 17.8, BioXcell), daily from treatment onset and until the last day of treatment. For cytokine secretion assays, mice were injected with 0.25 μg brefeldin A (Sigma-Aldrich) in the tail vein 24 h following BiCE treatment. Organs were collected 5 h later, and single-cell suspensions were produced. For the cDC1-depletion experiment, $XCR1^+$ cDC1s were depleted by intraperitoneal injections of diphtheria toxin starting 4 days following tumor inoculation, and during the entire treatment period, at a dose of 20 ng/g every other day, until 4 days after completion of the treatment course. Depletion efficiency was assessed by flow cytometry analysis.

For the LLC abscopal experiments, mice were inoculated simultaneously with two LLC tumors as described, one on each flank. Only the right flank tumor was treated by intertumoral injection (75μg BiCE or 30μg aPD-1), and the volume of both tumors was monitored.

For sLT-Ret experiments, Ret cells labeled with tdTomato were initially grown in RPMI medium. Their derivative (sLT-Ret) was generated by three cycles of isolation, culture, selection and re-injection of spontaneous lung metastasis of Ret cells. A total of 1×10^5 low-passage sLT-Ret cells were resuspended in PBS and mixed 1:1 with growth factor–reduced Matrigel (BD Biosciences) to a final volume of 50μL. Mice were injected intradermally at the right dorsal side, rostral to the flank, with a 29G insulin syringe (BD Biosciences). When tumor volume reached approximately 50 mm^3, mice were randomized to group with similar tumor size, and received treatment by intraperitoneal injection of PD-1 mAb (200μg), BiCE or bsAb control (500μg) at days 10, 13, 16. Tumors were measured 3 times weekly by caliper. Tumors were resected 18 days following injection. Lung metastases were monitored by CT imaging starting 3 weeks after primary tumor removal. Metastasis was quantified via FACS, by calculating the amount of sLT-Ret cells/lung following lung removal and perfusion on day 46.

OT-1 $CD8^+$ adoptive transfer in B16-OVA bearing mice

$CD8^+$ T cells were isolated from OT-I mice using $CD8^+$ T cell isolation kit (Miltenyi Biotech). Cells were expanded for 3 to 5 days using 100U/ml rIL2 and 2×10^6 CD3/CD28 beads (Miltenyi Biotech). After 10 days following tumor injection, 2×10^6 OT-1 $CD8^+$ T cells were adoptively transferred to C57BL/6J tumor-bearing mice by retro-orbital injection. Then, mice were treated with intraperitoneal injection of anti-mouse PD-1 mAb, BiCE or control PBS at days 11, 14, and 17.

In-vitro splenocyte dual binding assay

For the isolation of $CD8^+$ T cells and the induction of PD-1 upregulation, spleens were harvested from OT-I CD45.1 mice, and single-cell suspensions were prepared. Spleens were dissociated through a 70 μm nylon cell strainer, and then erythrocytes were lysed by 5 min incubation with red blood cell lysis buffer (Sigma-Aldrich) and washed with PBS. $CD8^+$ cells were isolated by negative selection using the EasySep Mouse $CD8^+$ T cell Isolation Kit (Stemcell) according to the manufacturer's protocol. Cells were then seeded at a concentration of $5x10^5$ in a 24-well plate and cultured in complete medium (RPMI 1640, 25 mM HEPES, 1% L-Glutamine, 10% FBS, 1% Pen Strep, 1% Non-Essential Amino acids, 1% Pyruvate and 0.05mM Beta-mercaptoethanol) with IL-15 (5 ng/ml, Peprotech), IL-7 (5 ng/ml, Peprotech), and 10 mg/ml OVA (257–264) peptide (Sigma-Aldrich). After 24 h, 10 mg/ml OVA was added to each well. Cells were cultured for an additional 48 h. Unstimulated controls were cultured in complete media with cytokines, but without OVA. Cells were evaluated for PD-1 expression by FACS, and after 48 h, 100% of cells were $PD\text{-}1^+$ relative to unstimulated controls. Once PD-1 expression was established, $PD\text{-}1^+$ $CD8^+$ T cells were incubated with splenocytes isolated from XCR1-cre-mTFP CD45.2 mice at a 1:10 ratio in U-shaped 96-well plates (ThermoFisher), at approximately $5x10^5$ cells/well. Cells were stained with LIVE/DEAD Fixable blue dead cell stain (ThermoFisher) followed by two washes with PBS, and then resuspended in 25 μL FACS buffer with mouse TruStain Fc block (BioLegened) and incubated for 15 min at room temperature. Cells were then washed twice and incubated with BiCE or control vehicle in 1:2 serial dilutions, for 1 h on ice in the dark. Cells were washed twice with FACS buffer, and surface antigens were stained in FACS buffer for 30 min on ice. Cells were washed twice, resuspended in 150 μL FACS buffer, and analyzed

by flow cytometry. Cell populations were defined by the following markers (BioLegend): $CD8^+$ T cells: $CD45.1^+$ (A20), $CD8^+$ (536.7). cDC1s: $CD19^-$ (1D3), $F4/80^-$ (BM6), $CD45.2^+$ (104), $CD11c^+$ (N418), and endogenous mTFP from XCR1-cre-mTFP mice. Doublets were normalized to cDC1 in each well.

Tissue processing for flow cytometry, imaging flow cytometry, PICseq and scRNA-seq

Tumor and tdLN were collected and subjected to mechanical and enzymatic digestion. Tumors were mechanically dissected into small fragments and transferred to GentleMACSTM C tubes (Miltenyi Biotec) with 0.33 mg/mL DNase I (Roche) and 0.27 mg/mL Liberase TL (Roche). Tumors were dissociated twice in the GentleMACSTM Octo Dissociator (Miltenyi Biotec) and the cell suspension was then incubated at 37°C, 25 rpm, for 40 min. Tumors were then dispersed through a 70 μm nylon cell strainer and washed with PBS. For lung dissociation, 40 mL of digestion solution was prepared for each mouse by adding 800 μL of Collagenase IV stock (0.2 mg/mL) and 200 μL of DNase I stock (0.05 mg/mL) to 39 mL of RPMI-1640 supplemented with 10% FBS. The harvested lung was then cut into small pieces, immersed in 1 mL of this solution, and incubated for 60 min at 37°C. After incubation, the tissue was dissociated, filtered through a 70 μm cell strainer, centrifuged, resuspended in ACK lysis buffer, and finally resuspended in FACS buffer for subsequent analysis. Lymph nodes and spleens were manually dissected through a 70 μm nylon cell strainer and washed with PBS. Spleens then underwent an additional step of RBC lysis (Sigma) for 5 min at room temperature, and were then washed in PBS. For the PICseq experiments, following dissociation, 15 tdLN were pooled for staining and FACS analysis.

Flow cytometry

Single cell suspensions were prepared as described above. For surface staining, cells were plated in U-shaped 96-well plates (ThermoFisher) at a concentration of $0.2\text{-}1x10^6$ cells in 100 μL PBS. Cells were first stained with LIVE/DEAD Fixable blue dead cell stain (ThermoFisher) followed by two washes with PBS, and then resuspended in 25 μL FACS buffer with mouse TruStain Fc block (BioLegened) and incubated for 15 min at room temperature. Surface antigens were stained in FACS buffer for 30 min on ice. Then, the cells were washed twice with FACS buffer, resuspended in 150 μL FACS buffer, and analyzed by flow cytometry. For intracellular staining, an additional staining step was performed using True-Nuclear transcription factor buffer Set Kit (BioLegened) according to the manufacturer's instructions. All samples were analyzed on CytoFLEX LX (Beckman Coulter). Unless otherwise specified, cell populations were defined by the following markers (BioLegened): cDC1s: $CD45^+$ (30F11), $CD19^-$ (1D3), $CD64^-$ (10.1), $F4/80^-$ (BM6), $CD11c^+$ (N418), MHC II^+ (M5/11415.2), $SIRP\alpha^-$ (P84), $XCR1^+$ (ZET). When XCR1 mAb was used in the experiment, cDC1 gating was as follows: $CD45^+$, $CD19^-$, $CD64^-$, $F4/80^-$, $CD11c^+$, MHC II^+, $Ly6C^-$ (HK1.4), $SIRP\alpha^-$. Migratory cDC1s were also $CD103^+$ (W19396D) while resident cDC1s were $CD103^-$. cDC2s: $CD45^+$, MHC II^+, $CD11c^+$, $CD19^-$, $CD64^-$, $F4/80^-$, $Ly6C^-$, $SIRP\alpha^+$. CD8 T cells: $CD45^+$, $CD11b^-$ (M1/70), $CD3^+$ (17A2), $CD8\alpha^+$ (536.7), $CD4^-$ (RM4-5). CD8 effectors were also $TCF1^-$ (BD, clone S33-966), $CD44^+$ (IM7), $CD62L^-$ (MEL14). CD4 T cells: $CD45^+$, $CD11b^-$, $CD3^+$, $CD8^-$, $CD4^+$, $FOXP3^-$ (MF14). Tregs: $CD45^+$, $CD11b^-$, $CD3^+$, $CD8^-$, $CD4^+$, $FOXP3^+$. T cell/cDC1 doublets were defined by the following markers: $CD45^+$, MHC II^+, $CD11c^+$, $CD19^-$, $CD64^-$, $F4/80^-$, $Ly6C^-$, $SIRP\alpha^-$, $CD3^+$. CD8/cDC1 doublets were gated as described, adding an additional gate for $CD8^+$. When staining for T–DC cytokine-secreting doublets or $TCF1^{+/-}$ doublets, their MFI was calculated using the doublet gating described above based on the expression of IFN-γ (XMG1.2) and IL-12 (C15.6). For absolute cell count, CountBright Absolute Counting Beads (Invitrogen) were used and calculated according to the manufacturer's protocol.

Imaging flow cytometry

Cells were first stained with LIVE/DEAD Fixable Violet dead cell stain (ThermoFisher) followed by two washes with PBS, and then resuspended in 25μL FACS buffer with mouse TruStain Fc block (BioLegened), and incubated for 15 min at room temperature. Cells were then washed twice, and surface antigens were stained in FACS buffer for 30 min on ice. Then the cells were washed twice with FACS buffer, resuspended in 30μL FACS buffer, and analyzed by imaging flow cytometry. Images were acquired by ImageStreamX mark II (Amnis, Part of Luminex, Au. TX) using a 60X lens (NA = 0.9). At least $2*10^5$ cells were collected from each sample. Lasers used were 405nm (120mW), 488nm (200mW), 561nm (200mW), 642nm (150mW) and 785nm (2mW). For the BiCE localization experiments, channels used were 1 (brightfield), 3 (CD11c), 6 (CD3), 7 (Vio Blue live/dead), 8 (MHC II), 9 (brightfield of 2nd camera), 11 (SAIVI Alexa Fluor 647), 12 (SSC). Images were analyzed using IDEAS 6.3 software (Amnis, Part of Luminex, Au. TX). Live cells were gated according their signal in the Live/Dead staining (Channel 7). Cell doublets were then gated according to the area vs. aspect ratio (the ratio between the minor axis and the major axis of a best-fit ellipse for the nuclear object) of the bright-field image. Cell populations were defined using the following markers (BioLegend): DCs: MHC II^+, $CD11c^+$. T cells: $CD3^+$. BiCE was labeled prior to injection with the SAIVI Alexa Fluor 647 Antibody Labeling Kit (ThermoFisher). Relevant doublets were gated as $CD3^+$ and MHC II^+ events. Cells were further selected based on the size of the MHC II-stained region (Area_M08) vs. the distance between the center of staining for CD3 and MHC II (Delta Centroid X Y_M06_CD3_M08_MHC II). An additional selection was made for cells that had the appropriate area and aspect ratio for both markers (CD3 and MHC II).

For BiCE localization experiments, cells positive for the antibody staining were selected for analysis from this population. To determine the interface region, morphology masks were created for CD3 (Ch6) and MHC II (Ch8). These masks were dilated by 4 pixels, and the interface between these two masks was defined as "Dilate(Morphology(M06, CD3), 4) and Dilate(Morphology(M08, MHC II), 4)". The intensity of the bispecific antibody staining (Ch11) in this region was calculated. To determine the ratio of the bispecific antibody in the interface relative to the rest of the cell membranes, the interface region was subtracted from the dilated CD3

and CD8 masks. From these subsequent masks, a mask for the interior of the cell (adaptive erode 70) was subtracted to delineate the membrane area of each cell. The antibody mean pixel intensity was calculated for the interface mask and for the combined membrane masks of both cells, and their ratio was calculated. To quantify the relative localization of the bispecific antibody, we used the Max Contour Position feature (defined as the location of the contour in the cell that has the highest staining intensity, mapped to a number between 0 and 1, with 0 being the object center and 1 being the object perimeter) on the CD3 and MHC II staining, either on single cells or within doublets.

BrdU proliferation assay in B16F10-bearing mice

B16F10 tumors were induced as previously described and allowed to grow for 11 days. Mice were then injected intraperitoneally with 1mg BrdU pulsing solution (BioLegend) and either BiCE or PBS. After 24 h, mice were sacrificed and the draining lymph nodes were taken for FACS staining using the Phase-Flow BrdU FITC kit (BioLegend), according to the manufacturer's protocol. Cells were additionally stained T–DC markers as previously described, and intracellularly with Ki67 (clone 16A8, BioLegend). Proliferating cells were calculated as the percent of cells expressing both BrdU and Ki67 from all $CD45^+$ immune cells.

B16F10 killing assay in B16F10-bearing mice

B16F10 tumors were induced as previously described and allowed to grow for 11 days. Mice were injected intraperitoneally with BiCE or PBS, and lymph nodes were taken after 24 h and digested. $CD8^+$ T cells were isolated as previously described and plated with $1*10^5$ B16F10 cells in 96-well U-shaped plates (ThermoFisher) at the indicated ratios. Cells were incubated for 24 h, and then single cell suspensions were prepared for FACS. Cells were first stained with LIVE/DEAD Fixable blue dead cell stain (ThermoFisher) followed by two washes with PBS, and then resuspended in 25μL FACS buffer with mouse TruStain Fc block (BioLegened), and incubated for 15 min at room temperature. Surface antigens (CD8, CD69) were stained in FACS buffer for 30 min on ice. Then, the cells were washed twice with FACS buffer, and an additional staining step was performed for intracellular staining of IFN-γ using True-Nuclear transcription factor buffer Set Kit (BioLegened) according to the manufacturer's instructions. All samples were analyzed on CytoFLEX LX (Beckman Coulter). B16F10 killing was calculated as the percent of dead $CD8^-$ cells from total $CD8^-$ tumor cell-line count, normalized to the killing assessed in control wells that were plated without CD8 cells.

Plate-based single-cell sorting

Cells were prepared for FACS as described above. In the B16-OVA tumor model experiment, cells were stained with CD8, CD45.1, CD45.2. Sorting was performed by gating for $CD8^+CD45.1^+$ for OT-1 $CD8^+$ T cells. In B16F10 tumor model experiments, cells were stained with TCRβ, CD45, MHCII, CD11b, and DAPI. Sorting was performed by gating for $TCR\beta^+CD45^+CD11b^-$ for T cells, and $CD45^+CD11c^+MHCII^+$ for DC. In the PICseq experiment, cells were stained with anti-human IgG, Ly6c, CD19, F480, CD11c, SIRPa, MHCII, XCR1, CD3 and CD8a. Sorting of PICs was performed by gating for $CD11c^+MHCII^+XCR1^+CD3^+$. Plate-based single-cell sorting was done using Symphony S6 (BD Biosciences) and analyzed using BD FACS DIVA software (BD Biosciences). Single cells were sorted into 384 capture plates prepared in-house that contained 0.1% Tris, RNAse inhibitor (Ribolock, Invitrogen), and 384 distinct RT primers. Promptly after sorting, plates were spun down to ensure immersion of cells into the lysis solution, snap-frozen on dry ice, and stored at −80°C until further processing. Flow cytometry datasets were analyzed using FlowJo software.

MARS-seq library preparation

Single-cell libraries were prepared using the massively parallel scRNA-seq method (MARS-seq), as previously described.[50] In brief, mRNA from cells sorted into 384 wall cell-capture plates were barcoded, converted into complementary DNA, and pooled. The pooled sample was then linearly amplified by T7 *in vitro* transcription. Subsequent RNA was fragmented and converted into a sequencing-ready library by tagging the samples with pool barcodes and Illumina sequences during ligation, reverse transcription, and PCR. Each cell library was tested for quality and DNA concentration.

MARS-seq processing

Single-cell RNA-seq libraries (pooled at equimolar concentration) were sequenced on an Illumina NovaSeq 6000 sequencer at a median sequencing depth of ~40,000 reads per cell. Sequences were mapped to the mouse genome (mm10). Demultiplexing and filtering were performed with the following adaptations: mapping of reads was performed using HISAT (v.0.1.6), and reads with multiple mapping positions were excluded. Reads were associated with genes if mapped to an exon, using the UCSC Genome Browser. Exons of different genes sharing a genomic position on the same strand were considered a single gene with a concatenated gene symbol. The level of spurious UMIs in the data was estimated using statistics on empty MARS-seq wells, with the exclusion of rare cases demonstrating estimated noise >5% (median estimated noise over all experiments was 2%).

MetaCell analysis

The R package MetaCell[51,52] was used to analyze the single-cell data as shown in Figures 1, 5, 6, S5 and S6. We first removed specific mitochondrial genes, immunoglobulin genes, ribosomal genes, and genes linked with poorly supported transcriptional models (such as those annotated with the suffix "Rik"). Cells with less than 300 UMIs were discarded from the subsequent analysis. Informative genes with high variance to mean were selected using the variance-to-mean parameter T_vm > 0.1 and minimum total UMI

count >100. To construct the metacells, we used standard parameters with K = 100 and 750 bootstrap iterations to resample 75% of the cells in each iteration to ensure homogeneity within each metacell. Cells across all treatment conditions were combined for metacell construction. Metacells were then manually annotated based on analysis of marker genes and known cell type markers.

In the initial clustering of the metacells, the major clusters of myeloid and lymphoid cells were identified, as well as one doublet contamination. The myeloid and doublet metacells were removed, and the lymphoid clusters were manually annotated. We combined the clusters if there were no significant differences in their marker genes, and annotated them with established cell-type markers (e.g., Foxp3 – Treg, Cd69 – ActivatedCD4, Tcf7 – NaïveMemory CD8 and so on).

The 2D projection of metacells was computed using a force-directed layout algorithm on the regularized similarity metacell graph GM, as described in the MetaCell algorithm. For the single cell projection, first we computed a raw similarity matrix using Pearson's correlation, and then constructed a weighted adjacency matrix to define a directed cell graph, G. Cells were then positioned by taking the average metacell coordinates of filtered neighbor cells from G.

Analysis of the DC recruitment module

To define a signature gene set for the DC recruitment module from the CD8 transcriptional manifold, we calculated the Pearson correlation of all feature genes to the selected anchor gene Xcl1, over the effector-early and IFN-γ^{high} effector metacells (UMI fractions) scores. Selecting a gene set starting from a well-defined literature-based anchor ensured that our module was based on the pathway of interest, and focusing on effector-early and IFN-γ^{high} effector metacells directed the gene set to the DC recruitment behavior in effector CD8 cells, rather than the correlation of genes across the naive to effector spectrum. The DC recruitment module score is defined as the sum of UMI fractions across metacells of the 25 most highly correlated genes. The average score per mouse was calculated as the weighted mean of all metacells containing cells from a given mouse. Control and aPD1 treated mouse scores across days 2 and 5 post-treatment were compared to study the effect of aPD1 treatment on the DC recruitment module.

PIC-seq summary

Assignment of PICs to their T cell and DC identities was performed as previously described with necessary adjustments.[28,36] PICs were modeled as a linear mixture of pairs of contributing cells. Each contributing cell (T cell or myeloid) belongs to a metacell from the respective T cell or myeloid background models calculated over the singlet populations, and its gene expression is sampled from the multinomial probability distribution of that metacell. The mixing factor, α, assigned for each PIC, denotes the fraction of UMIs contributed by the T cell to that PIC.

The PIC-seq algorithm operates in two steps. First, it applies a linear regression model trained on synthetic PICs to infer α for each PIC. Second, it constructs all possible combinations of metacells from populations A and B mixed by α, and calculates the expected gene expression distributions of these mixtures. A maximum likelihood estimator is applied on each PIC, to derive two metacells whose combination is most likely to give rise to the PIC.

MetaCell model of tdLN from B16F10 tumor-bearing mice

We derived a MetaCell cover of $CD3^+$ T and $MHCII^+CD11c^+XCR1^+$ myeloid cells from pooled tdLN OF B16F10 tumor-bearing mice. Mitochondrial and ribosomal genes were removed from the UMI tables. Gene features for MetaCell covers were selected using the parameters Tvm = 0.25, total UMI >300, and more than three UMIs in at least three cells. MetaCell was used to build a k-NN graph, perform boot-strapped co-clustering (100 iterations; resampling 70% of the cells in each iteration) and derive a cover of the co-clustering k-NN graph (K = 30, minimum metacell size = 20). Detailed annotation of the different T and myeloid subsets was performed by analysis of enriched genes according to the literature.

PIC-seq analysis of the mouse model

To choose gene features for estimating the mixing factor, we first removed those with a strong cell-cycle signature and computed the correlation with cell size as described above, retaining 464 genes. The R2 value was 61%. Feature selection for the MLE assignment was performed similarly to PIC-seq of human tumors, resulting in 337 genes used as features. To validate the MLE assignment, we computed the error in assignments over 5,000 synthetic PICs.

Comparing observed and expected expression

The expected levels of a gene in each PIC were reconstructed as previously described.[28,36] The expected expression of each gene in a given PIC equals the α-weighted sum of the contribution from the T cell part (which can be estimated from the characteristic multinomial distribution of the contributing T metacell) and the contribution from the myeloid cell part. We used an FDR-adjusted chi-squared test to systematically scan for genes whose observed values diverged from expected values in specific groups of PICs ($q < 10^{-4}$ in mouse PICs).

Proliferation analysis

To define a set of proliferative genes in the data, we used anchor genes (Top2a, Tubb5, Mki67) to identify highly correlated proliferative genes (with Spearman's rho correlation >0.75). We used this set of genes to calculate the average log2 footprint expression per metacell and set a stringent cut-off of proliferation score >0.5 for downstream analysis.

Ligand-receptor analysis

To investigate the downstream effect of BiCE treatment on the interaction between CD8 subpopulations and DCs, we employed MultiNicheNet[58] to identify putative ligands and receptors that mediate the interaction. To this end, we defined CD8 subpopulations as sender cells and DC subpopulations and TAMs (since TAMs are major drivers of the immunosuppressive TME) as receiver cells. Potential ligands were extracted if they were expressed in at least 5% of the sender cells within their respective clusters and the p value cut-off was set to of 0.05. We prioritized the predicted ligand-receptor interactions with the default prioritization weights and visualized the top 50 interactions across the two treatment conditions using circus plots in Figure 5.

QUANTIFICATION AND STATISTICAL ANALYSIS

Flow cytometry data analysis was performed using FlowJo v.10.6.2; all other data analyses were performed using GraphPad Prism (GraphPad Software). Quantitative data are presented as means ± SEM unless otherwise indicated. When geometric mean intensity is presented, the MFI is shown; in cases where the value is the fluorescence intensity of the Ab relative to an isotype control, delta geometric mean intensity is presented (ΔMFI). Although no statistical method was used to predetermine sample size, mouse numbers were taken into consideration for *in vivo* studies to ensure that biological effects would be detected, and to enable comparison between groups, and were determined based on results of preliminary experiments. scRNA and FACS experiments were done in groups of at least 5 mice, while tumor growth experiments were performed in groups of at least 10 mice due to the inherent heterogeneity in these experiments, unless otherwise noted. Group allocation was randomized for all *in vivo* experiments, as described above, and tumor measurements were performed blindly. For *in vitro* studies, researchers were not blinded to the identity of the groups when performing the experiments. For each dataset, the normality of the population and/or population residuals (Gaussian distribution) was confirmed using Shapiro–Wilk and/or D'Agostino–Pearson testing. For normal distributions, one-way analysis of variance (ANOVA) with Tukey's post hoc test was used to compare all groups with three or more treatments. When two groups were compared, an unpaired two-tailed Student's *t* test (two-tailed, unequal variance) was used to determine statistical significance. When data were not normally distributed, a nonparametric test was used, either Kruskal–Wallis with Dunn's post hoc test for multiple comparisons or Mann–Whitney test when two groups were compared. Statistical significance is indicated in all figures as follows: $*p \leq 0.05$, $**p \leq 0.01$, $***p \leq 0.001$, $****p < 0.0001$, ns: non-significant.

Supplemental figures

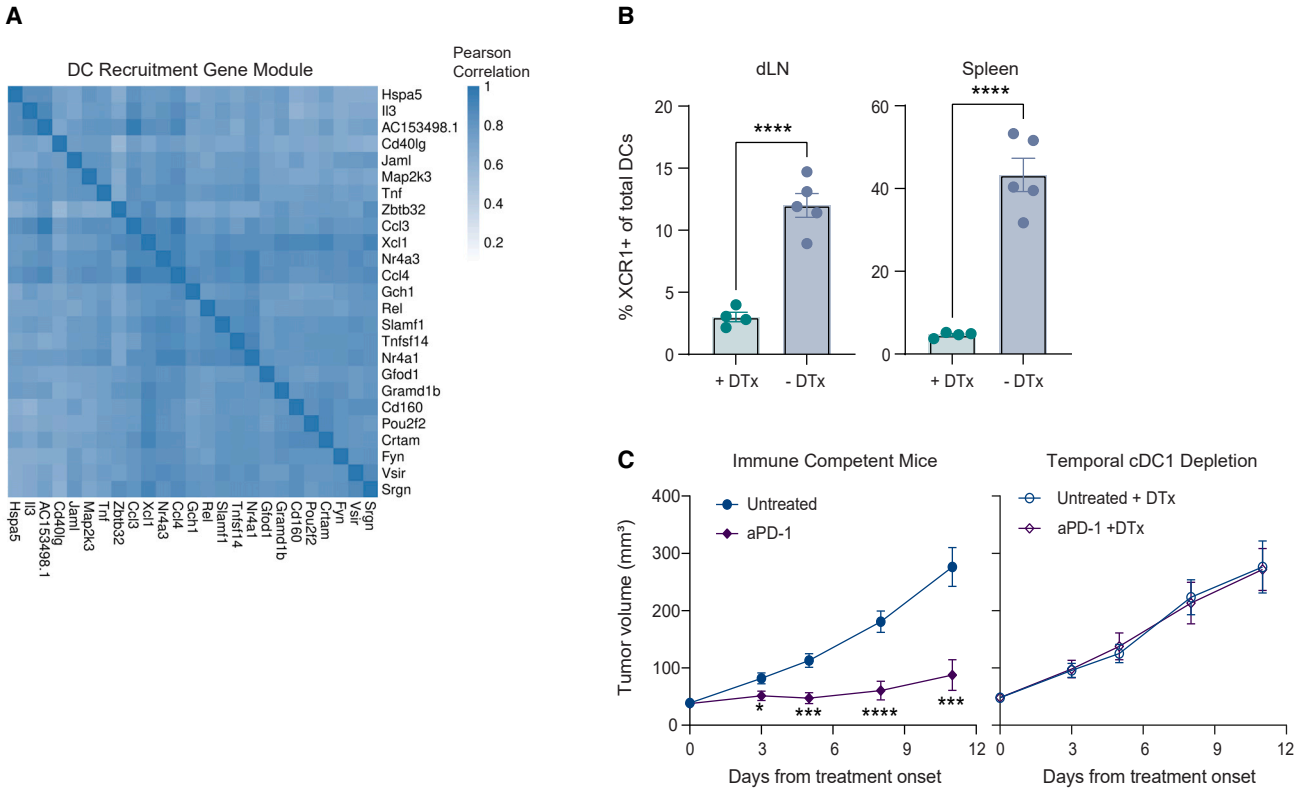

Figure S1. cDC1s mediate T cell efficacy during anti-PD-1 immunotherapy

(A) Pearson correlation of the DC recruitment (DC-r) gene module described in Figure 1 based on correlation with the expression of Xcl1 in the effector-early and IFN-γ^{high} effector states of the $CD8^{+}$ manifold.

(B) Barplots of XCR1+ cell frequencies in XCR1-iDTR mice following DTx injection in the dLN and spleen, compared to control. Each dot represents an individual mouse.

(C) Tumor growth rate of MC38 tumor cells in XCR1-iDTR mice treated with PD-1 mAb, with or without DTx injections for temporal cDC1 depletion. n = 20 mice; combined data from two independent experiments are shown.

Unless otherwise stated, results are presented as means ± SEM. Stars indicate a significant p value as calculated by the relevant statistical test. Related to Figure 1.

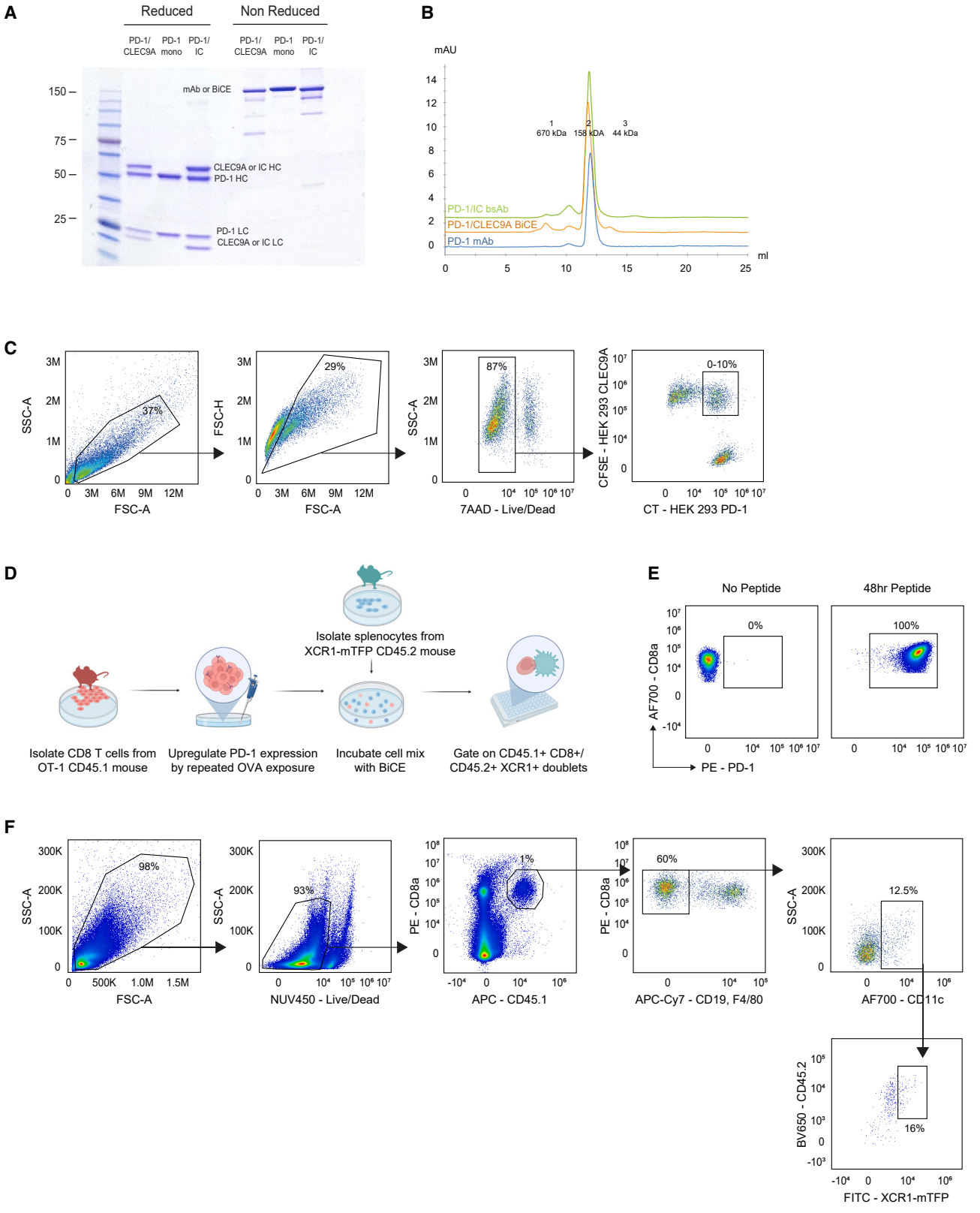

(legend on next page)

Figure S2. Design and characterization of the Bispecific DC-T Cell Engager (BiCE)

(A) SDS-PAGE of the indicated reduced and non-reduced bsAb proteins and controls. HC- heavy chain; LC- light chain. MW marker (kD) was loaded in the left lane.

(B) Size-exclusion chromatography of the indicated proteins.

(C) Gating strategy for HEK293-based bridging assay, shown in Figure 2C.

(D) Illustration of the experimental workflow of the splenocyte-based cell bridging assay, shown in Figure 2D.

(E) Flow cytometry analysis of PD-1 expression by $CD8^+$ cells isolated for the bridging assay shown in Figure 2D.

(F) Gating strategy for BiCE splenocyte assay to identify the CD8/cDC1 doublets plotted in Figure 2D. Related to Figure 2.

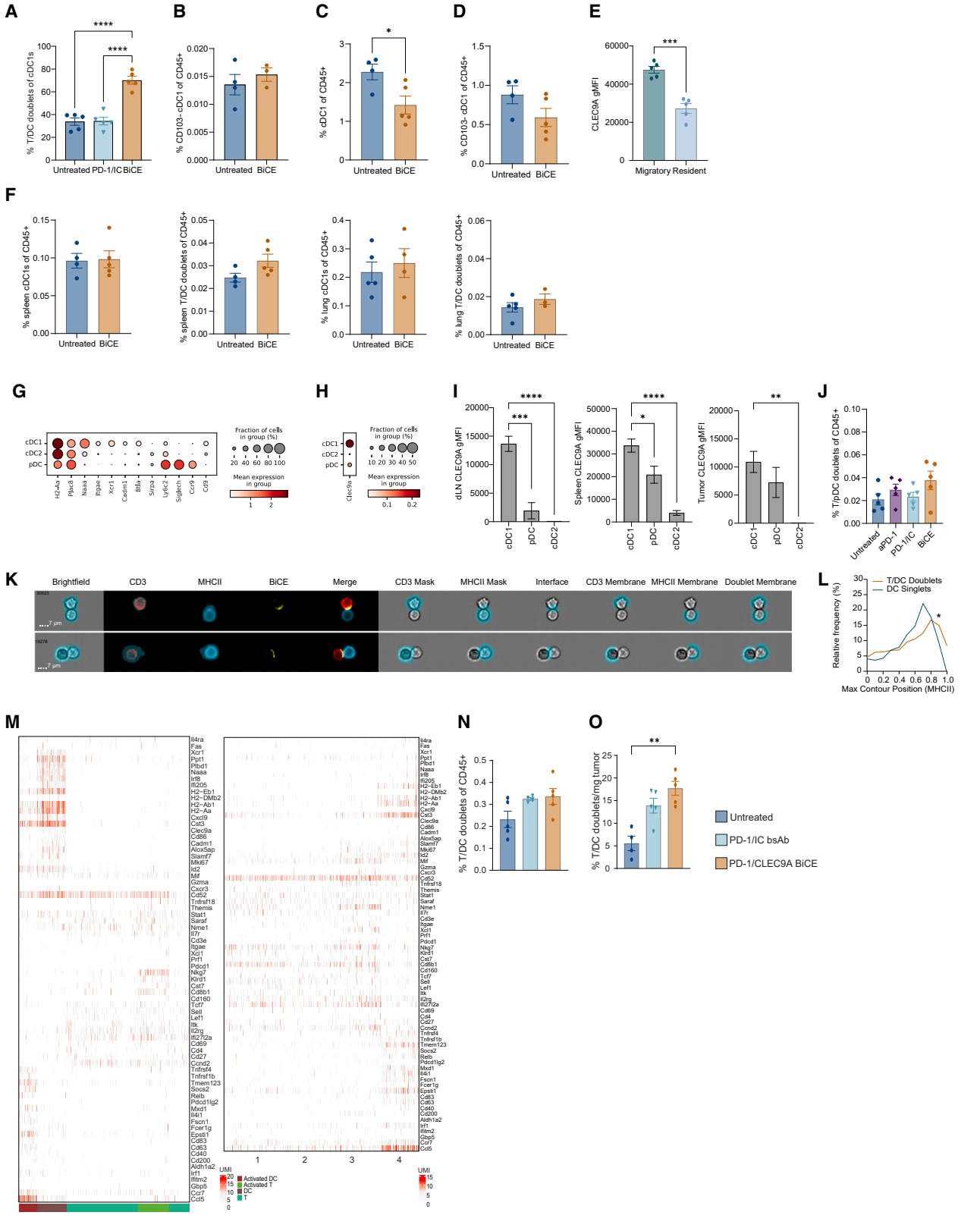

(legend on next page)

Figure S3. BiCE forms activated DC-T cell conjugates

(A) T–DC doublet frequencies in the tumor-draining lymph nodes of B16F10-bearing mice 24 h following BiCE injection. Each dot represents a single mouse; one independent experiment of three replicates is shown.

(B) Frequency of $CD103^-$ cDC1s in the dLN calculated by flow cytometry 24 h following treatment. Each dot represents a single mouse; one independent experiment of two replicates is shown.

(C) cDC1 frequencies in the tumors of B16F10-bearing mice 24 h following treatment. Each dot represents a single mouse; one independent experiment of two replicates is shown.

(D) Frequency of $CD103^-$ cDC1s in the tumor 24 h following treatment. Each dot represents a single mouse; one independent experiment of two replicates is shown.

(E) Membranal CLEC9A expression level of migratory vs. resident cDC1 in the dLN of B16F10-bearing mice. Each dot represents a single mouse; one independent experiment of two replicates is shown.

(F) cDC1 and T–DC frequencies in spleens and lungs, 24 h following treatment. Each dot represents a single mouse; one independent experiment of two replicates is shown.

(G) Dotplot showing the normalized expression of selected markers for dendritic cell subpopulations from $CD45^+$ MC38 and B16F10 tumors. Dot size represents the percentage of cells expressing the respective gene and color denotes the scaled mean gene expression per cell type as determined by scRNAseq.

(H) Dotplot showing the normalized expression of Clec9a in dendritic cell subpopulations as determined by scRNAseq using cells collected from $CD45^+$ MC38 and B16F10 tumors.

(I) Membranal CLEC9A expression levels in dendritic cell subpopulations in the dLN, spleen and tumors of untreated B16F10 tumor-bearing mice as determined by flow cytometry. n = 4–5 mice; one independent experiment of two replicates is shown.

(J) T/pDC doublet frequencies in the tumor-draining lymph nodes of B16F10-bearing mice following BiCE treatment. Cell doublets were calculated as the percentage of pDC/CD3 pairs from total immune cells. Each dot represents a single mouse; one independent experiment of three replicates is shown.

(K) Imaging flow cytometry analysis of the indicated cells following BiCE treatment. Each cell type in the doublet and their interface was defined using Mask morphologies. The cell membranes were delineated, and the interface was subtracted to calculate BiCE intensity at the cell membrane or at the interface itself.

(L) BiCE localization relative to the cell membrane as calculated by determining the Max Contour position for $MHCII^+/CD3^+$ doublets compared to MHCII+ singlets. n = 3 mice; one independent experiment of three replicates is shown.

(M) Gene expression profiles of singlet T cells and DC (left) and PICs (right) grouped by their MetaCell and PIC-seq assignment to T cell and DC subsets.

(N) Evaluation of T–DC doublets in the dLN 4 days after treatment initiation. Dots represent individual mice.

(O) Evaluation of T–DC doublets in the tumor 1 day after treatment initiation. Dots represent individual mice. For (N-O), one representative experiment of three is shown.

Unless otherwise stated, results are presented as means ± SEM. Stars indicate a significant p value as calculated by the relevant statistical test. Related to Figure 3.

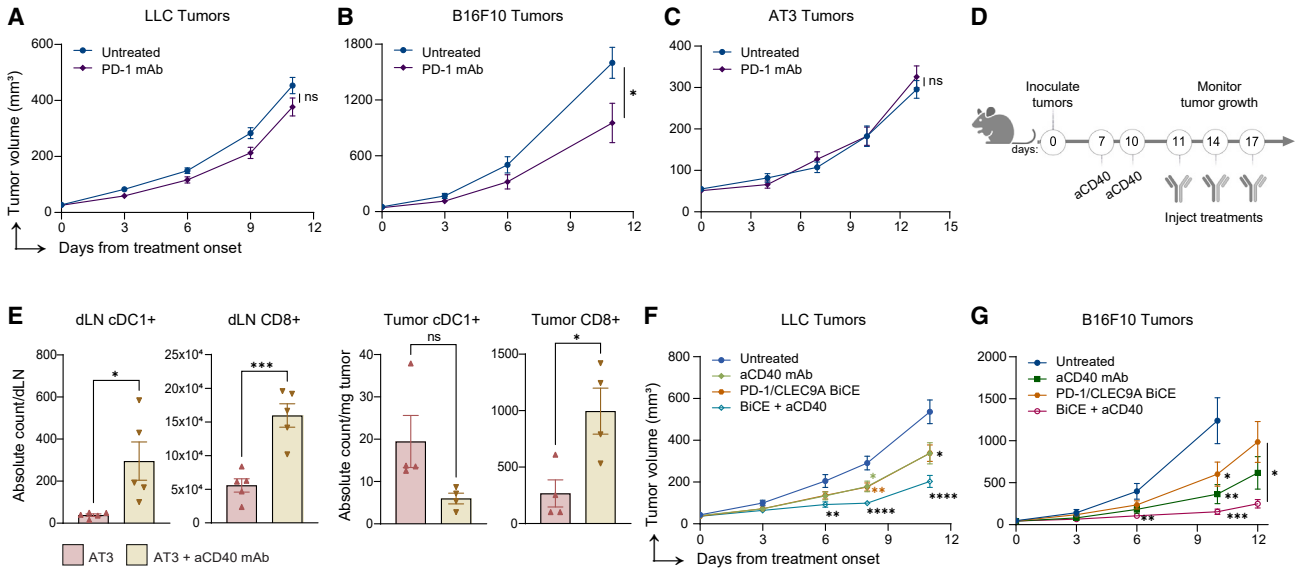

Figure S4. BiCE promotes antitumor activity

(A) Tumor growth in LLC-bearing mice was monitored following the indicated treatments. n = 10 mice; one representative experiment from three independent replicates is shown.

(B) Tumor growth in B16F10-bearing mice was monitored following the indicated treatments. n = 10 mice; one experiment is shown.

(C) Tumor growth in AT3-bearing mice was monitored following the indicated treatments. n = 10 mice; one independent experiment of two replicates is shown.

(D) Illustration of the antitumor experimental workflow of the data presented in Figure 4D.

(E) Flow cytometry analysis of $CD8^+$ T cells and cDC1 numbers in mice bearing AT-3 tumors following the aCD40 priming. Absolute cell count/dLN or absolute cell count/mg tumor is shown; dots represent individual mice.

(F) Tumor growth in LLC-bearing mice was monitored following the indicated treatments. n = 10 mice; one experiment is shown.

(G) Tumor growth in B16F10-bearing mice was monitored following the indicated treatments. n = 10 mice; one independent experiment of two replicates is shown.

Unless otherwise stated, results are presented as means ± SEM. Stars indicate a significant p value as calculated by the relevant statistical test. Related to Figure 4.

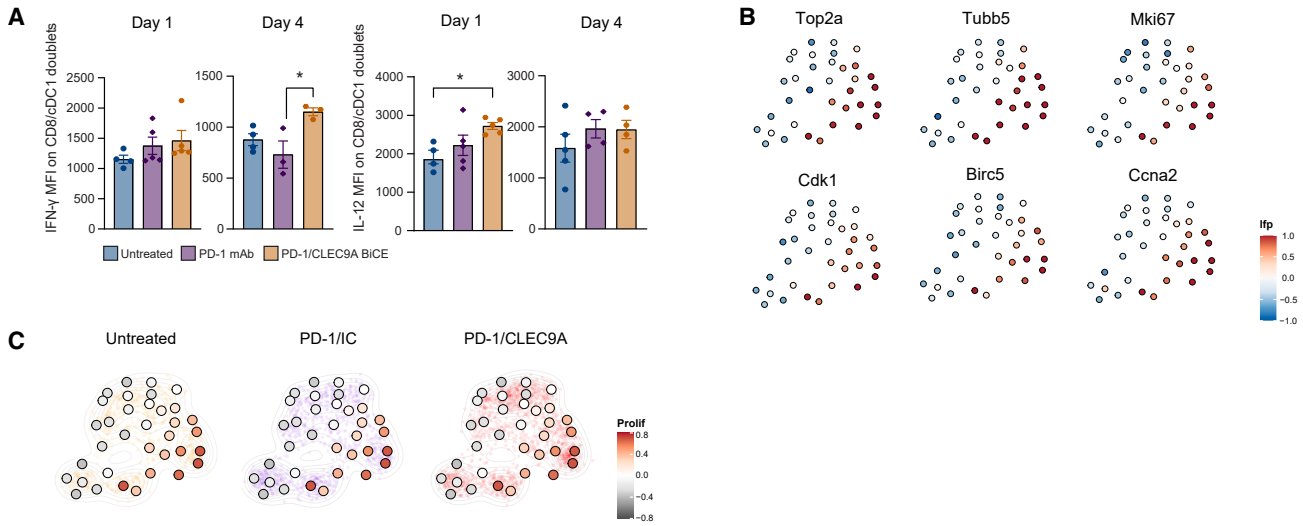

Figure S5. BiCE-mediated crosstalk enhances T cell activation and proliferation in the TME

(A) Evaluation of IL-12 and IFN-γ levels in $CD8^+$ T cell/cDC1 tumor doublets 1 day and 4 days following treatment. Dots represent individual mice; one representative experiment of two replicates is shown.

(B) Gene expression heatmap of top selected proliferation genes from the lymphoid clusters shown in Figures 5C and 5D.

(C) Proliferation score projected on the metacells with separate panels for each of the treatment conditions. The dots and contour show the single cells for each treatment respectively.

Unless otherwise stated, results are presented as means ± SEM. Stars indicate a significant p value as calculated by the relevant statistical test. Related to Figure 5.

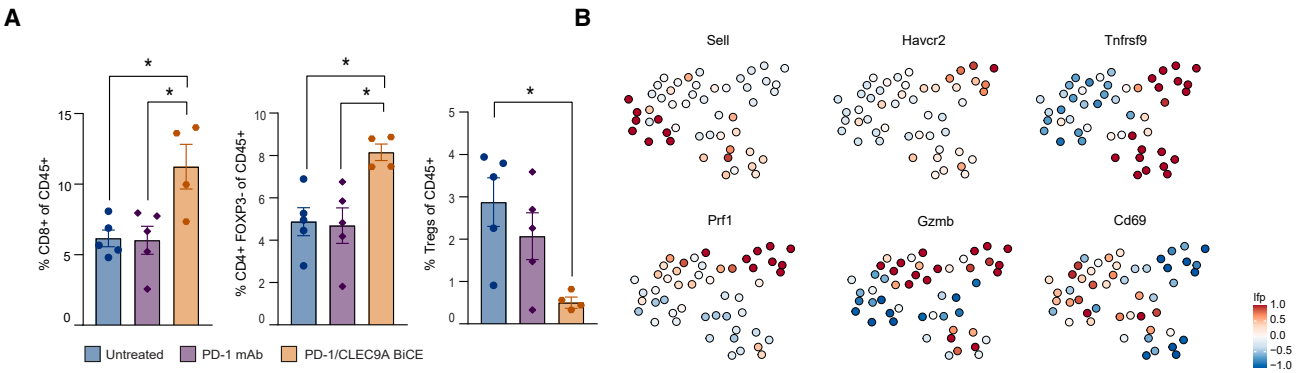

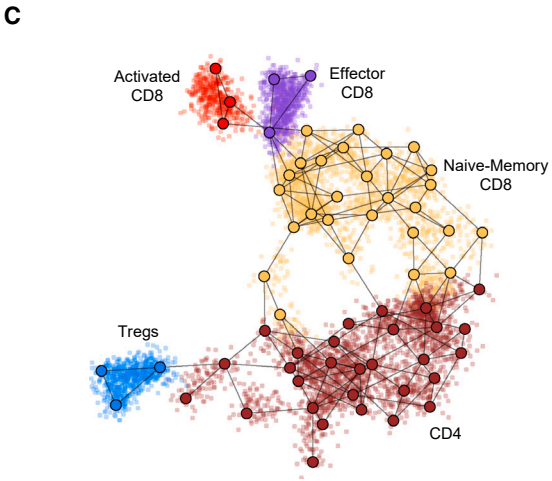

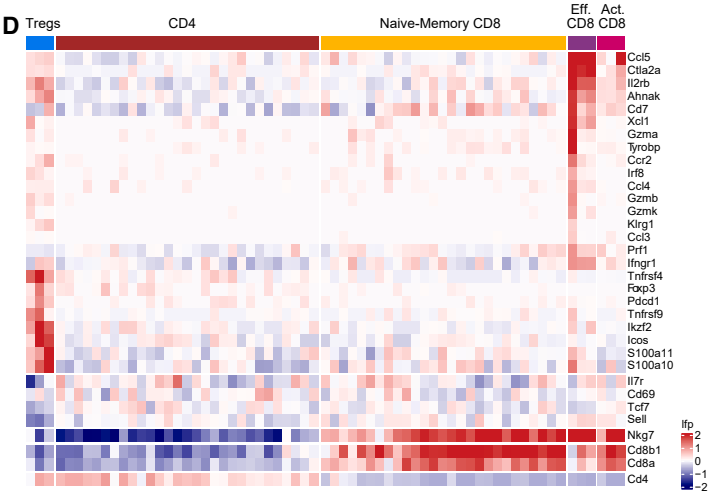

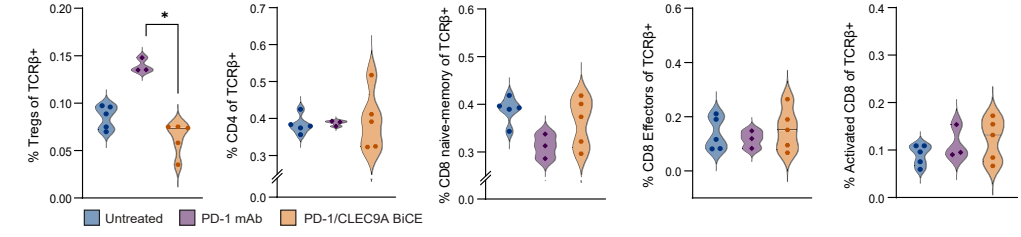

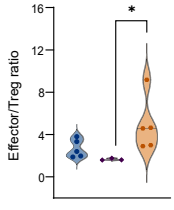

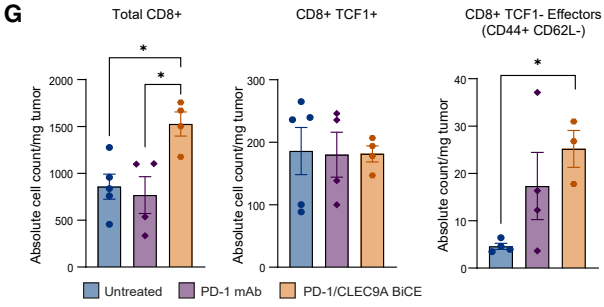

(legend on next page)

Figure S6. BiCE modulates TILs

(A) Frequencies of the indicated T cell subsets evaluated by flow cytometry from B16F10 tumors harvested 5 days following the final BiCE injection. Data used to calculate the effector/regulatory ratio are shown in the left panel of Figure 6A. Dots represent individual mice; one representative experiment of three is shown.
(B) Projection of key marker genes onto T cell clusters in the tumor metacell analysis.
(C) Two-dimensional graph projection of 65 metacells representing 6530 single-cells sorted from TCRβ gates from dLN.
(D) Gene expression heatmap of top selected genes from the lymphoid clusters in the dLN.
(E) Violin plots showing the proportion of T cell clusters over the TCRβ gated cells among the different treatment conditions in the dLN. Each dot represents an individual mouse.
(F) Violin plot showing the ratio of activated CD8 T cells and effector CD8 cells over Tregs per treatment condition in the dLN. Each dot represents an individual mouse.
(G) Quantification of absolute numbers of the indicated cell types from harvested tumors 4 days following treatment initiation. Each dot represents an individual mouse; one representative experiment of three is shown.
Unless otherwise stated, results are presented as means ± SEM. Stars indicate a significant p value as calculated by the relevant statistical test. Related to Figure 6.